Diffusion MRI for Brain Connectivity Mapping and Analysis

Brian G. Booth and Ghassan Hamarneh

Contents

1 Diffusion Weighted Image Acquision

Diffusion MRI (dMRI) is a powerful imaging protocol that allows for the assessment of the organization and integrity of fibrous tissue. The imaging works by measuring the diffusion of water molecules within the body. This diffusion is restricted by cell membranes and as a result, rates of diffusion are far less across tissue fibers than parallel to them. With enough diffusion measurements along different directions in 3D, we can non-invasively obtain a model of the diffusion pattern at different points within an imaged subject.

The diffusion patterns measured using dMRI have had a significant impact on the analysis of neural connectivity within the white matter of the brain. Neural pathways, dubbed fiber tracts, can be traced out from the directional information from the diffusion patterns. This process is known as tractography and due to noise, motion artifacts, and partial voluming effects, is a computationally difficult problem.

We present here an examination of the current state of tractography and diffusion MRI[1]. In particular, we look at the computational challenges inherent in this area and the open problems that remain.

1.1 Biological Basis for Diffusion MRI

The biological basis for diffusion MRI dates back to 1828 when botanist Robert Brown noticed the continuous and random motion of pollen grains suspended in water [39]. What Robert Brown had discovered was later determined to be the motion of water molecules due to thermal agitation [69]. This motion, now known as Brownian motion or diffusion, was later characterized by Albert Einstein [51], resulting in Einstein's equation:

$$r^2 = 6dt. \tag{1}$$

What Einstein's equation characterized was that the square of the average displacement of molecules (r) with a given diffusion rate (d) is proportional to the observation time (t). If we can measure this molecular displacement over a fixed time, we can obtain the diffusion rate of different substances under different conditions.

As the majority of the human body is water [57], the diffusion phenomenon occurs within us as well. While the diffusion process is random, our cell structures can restrict or hinder the the motion of water molecules [20]. As such, the diffusion of water molecules in our body depends on the microstructure of our tissues. Fast molecular diffusion occurs within and around a cell as there are few microstructures to inhibit motion. Diffusion though the cell however is slower as the cell membrane and other structures (*e.g.,* myelin sheaths in the brain white matter) restrict molecular motion.

Since the diffusion of water within the body is dependent on local cell structure, we can discuss how different organizations of these structures affect diffusion rates. Consider for example the human brain where functional regions (gray matter) are connected by a collection of neural pathways (white matter). Figure 1 presents diffusion measures for the brain's corticospinal fluid (CSF), gray matter, and white matter respectively. When the cell structure is minimal as in CSF, we see fast

[1]This chapter is an updated version of the one we published in [34].

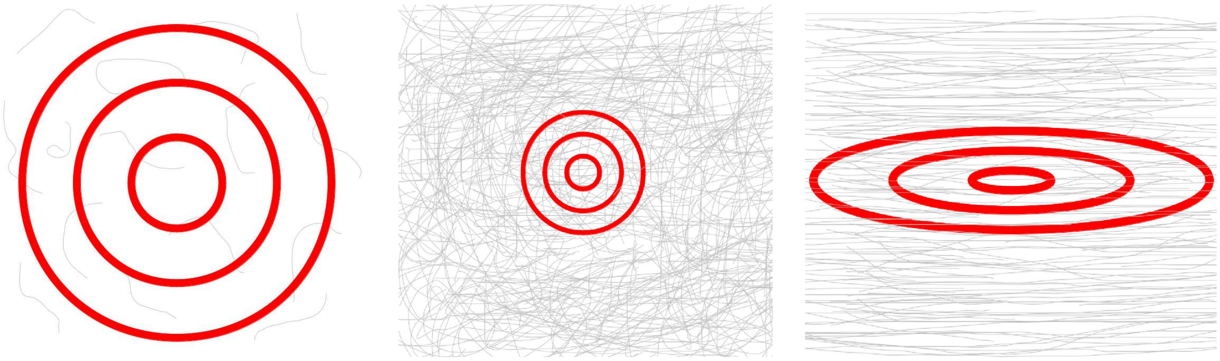

Figure 1: Synthetic examples of the diffusion seen in Corticospinal fluid (left), gray matter (middle), and white matter (right) within the brain. The diffusion rates for various directions are shown in red. Adapted from [4].

isotropic diffusion. More complex cell structure that is not consistently organized, such as gray matter, shows slower, but still isotropic, diffusion. Yet if the local cell structure is organized along a consistent orientation, as it is in white matter, the diffusion rates become anisotropic, *i.e.,* they vary with regards to direction [20].

These diffusion differences within the brain are potentially useful cues in analyzing brain structure and function. For example, measuring the average diffusion rate or the anisotropy of a tissue can give us significant information about the tissue's organization and integrity [91]. Diffusion measurements would be most informative in white matter regions where the orientation of the microstructure can be inferred from the diffusion. This microstructural orientation within the brain's white matter is, in turn, known to describe the direction of neural pathways in the brain [21]. As a result, by measuring the diffusion using Einstein's equation, we could infer the orientational structure of the brain's white matter and ultimately, map out the brain's neural pathways. This is precisely what diffusion MRI is used to accomplish.

1.2 Diffusion Weighted Image Acquisition

To understand how diffusion can be measured through magnetic resonance imaging, we must first address the basic concepts on nuclear magnetic resonance. The most fundamental of those concepts is the physical property of spin (s) that all elementary particles possess. An example of a particle's spin is shown in Figure 2. The spin property rotates the particle around its nucleus, thereby giving the particle a magnetic moment (m). This magnetic moment can then be manipulated using magnetic fields like those generated by an MRI scanner. As the body is mostly water, the spins of hydrogen atoms within water molecules become a good candidate for MR imaging.

1.2.1 Magnetic Resonance Imaging

Magnetic resonance imaging manipulates the magnetic moments of hydrogen atoms in a specific pattern in order to generate an image of tissue measurements. This pattern consists of three principal steps: precession, resonance, and relaxation. We consider each in turn.

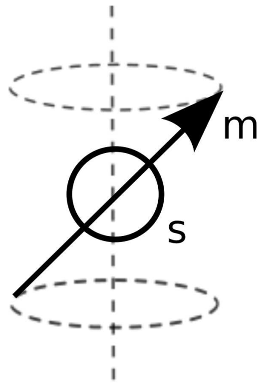

Figure 2: Nuclear spin s generating a magnetic moment m. The particle spins around a rotational axis shown here in gray. Adapted from [79].

Precession: A static magnetic field $\mathbf{B}_0$ is applied to the body. This magnetic field aligns the rotational axis of each spin with its field direction. These spins now rotate (*i.e.,* precess) around the same magnetic axis. Note that roughly an equal number of spins will be aligned with the positive direction of the magnetic axis as with the negative direction and the overall signal generated during precession will be negligible.

Resonance: With the magnetic field $\mathbf{B}_0$ in place, a second, weaker, magnetic pulse is applied to the body in the direction g. This second field results in the magnetic moment m of each spin aligning with the pulse direction g. The spin's axis of rotation remains aligned with $\mathbf{B}_0$. The result of the resonance phase is to cause the net magnetism of the spin to veer away from the main magnetic field $\mathbf{B}_0$.

Relaxation: The second magnetic pulse is removed and the magnetic moments of the hydrogen atoms realign with $\mathbf{B}_0$. As this realignment occurs, the changing magnetic field generated by the realignment of the spins induces a current in the coil of the MRI scanner. From this current, two common measurements can be taken:

1. Spin-spin relaxation time (T_2): The amount of time it takes for the magnetism in the direction of g to reduce to 37% of its maximum value.

2. Spin-lattice relaxation time (T_1): The amount of time it takes for the magnetism in the direction of $\mathbf{B}_0$ to recover 63% of the magnetism it lost when the second gradient was applied in the direction g.

These relaxation times can be visualized at multiple locations in the brain, resulting in what are known as T_1 and T_2 weighted images.

1.2.2 Diffusion Weighted Imaging

Since MR imaging depends on the magnetic moments of hydrogen atoms, it is possible to develop a sequence of precession, resonance, and relaxation periods that allow MRI to measure the movement of hydrogen atoms over time, and in turn the water molecules of which they are a part. Such

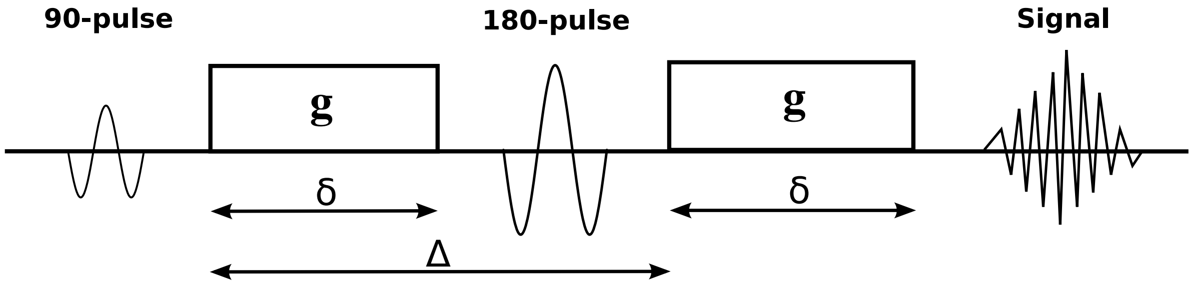

Figure 3: The Stejkall-Tanner diffusion weighted imaging sequence. Adapted from [120].

a imaging sequence was initially described by Stejskal and Tanner [110], and later adapted to the scanning of the human body by Le Bihan and Breton [26]. This imaging sequence is summarized in Figure 3 for a given diffusion direction $\mathbf{g}$.

The sequence in Figure 3 assumes the magnetic field $\mathbf{B}_0$ has been applied and that the spins are precessing around $\mathbf{B}_0$. In this state, a magnetic pulse is applied at an angle of $90°$ from the direction of $\mathbf{B}_0$. This pulse aligns the spins that were separately aligned to either the positive or negative $\mathbf{B}_0$ axis. Once the spins are aligned, the $90°$ pulse is removed an a second pulse, known as a gradient pulse, is applied in the direction $\mathbf{g}$. This gradient pulse senses the induced current to a specific angular direction.

A third magnetic pulse in the direction $180°$ from $\mathbf{B}_0$ follows the gradient pulse and then the gradient pulse is reapplied. The $180°$ pulse plays a key role in that it flips the spin direction of the atoms to the opposite of what they were during the precession phase. As a result of this flip, the current induced by stationary atoms during the application of the second gradient pulse will cancel out the current induced by the same atoms during the first gradient pulse [79]. Therefore, the resulting signal measured after all gradient pulses have been applied relates solely to the molecules experiencing motion in the direction $\mathbf{g}$.

The T_2 relaxation time is then measured from this final signal for multiple locations in the brain and visualized in what are known as diffusion weighted images. Figure 4 displays a conventional T_2 image next to sample diffusion weighted images (DWIs) for various gradient directions $\mathbf{g}$. Note here that rapid diffusion results in fast T_2 relaxation times, resulting in a low intensity in the diffusion weighted image. Further note the different rates of diffusion for different directions within the brain's white matter as pointed out by the white arrows in Figure 4.

From the diffusion weighted image for gradient direction $\mathbf{g}$, the diffusion rate (d) can be computed using the Stejskal-Tanner equation:

$$S = S_0 \exp(-bd) \tag{2}$$

where S is the diffusion weighted image intensity, S_0 is the standard T_2 image intensity, and b is the diffusion weighting [110]. The diffusion weighting b is in turn proportional to the strength and duration of the gradient pulse. The T_2 image used in (2) is typically referred to in this context as a $B0$ image as it is acquired without the application of the gradient pulses (*i.e.,* $b = 0$). The scalar d is commonly referred to as the apparent diffusion coefficient (ADC).

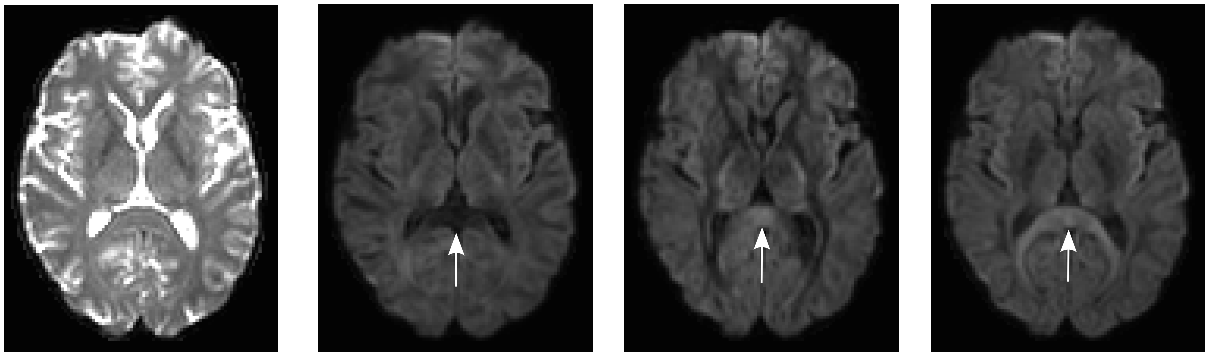

(a) $B0$ Image (b) Diffusion Weighted Images

Figure 4: Axial slices of (left to right) (a) standard T2 image and (b) its corresponding diffusion weighted images from gradient pulses in the horizontal, vertical, and out of plane directions. Note the differences in measured diffusion in the Splenium due to gradient direction (highlighted by the white arrows). Adapted from [69].

1.3 Correction of Image Artifacts

While dMRI provides us with measurements of diffusion, it must be acknowledged that the quality of the diffusion weighted images is affected and limited by the image acquisition process. All further analysis is going to depend on the accuracy of these diffusion measurements and as such, we must address the presence of noise and imaging artifacts within these diffusion weighted images.

Diffusion MRI is susceptible to various artifacts, the three most common being eddy currents, subject motion, and Rician noise [14]. Let us consider each in turn.

1.3.1 Eddy Currents

As seen in the diffusion imaging sequence in Figure 3, multiple magnetic gradient pulses are applied in rapid succession. Switching between these gradients can result in fluctuations in the scanner's magnetic field. These fluctuations induce what are known as eddy currents in the coil of the MRI scanner. The eddy currents interfere with the currents induced by the scanned subject, thereby distorting the resulting diffusion weighted images [14].

Much is known of eddy currents, namely that they are dependent on the magnitude of the gradient pulse, independent of the subject being scanned, and that they result in related geometric and intensity distortions in diffusion weighted images [62]. The geometric distortion produced from eddy currents has been shown to consist of a translation, scale and shear of the resulting image and is commonly rectified using affine registration [62, 84, 29]. The diffusion weighted images are corrected by registering them to a T_2 weighted image with the mutual information similarity measure providing the best results [84]. As the T_2 image is acquired without gradient pulses that produce eddy currents, it is assumed to be free of geometric distortion, thereby making it an appropriate template to which we can register the DWIs. Intensity corrections are then calculated directly from the magnitudes of the shear, scaling, and translations of the affine warp [62, 84].

One benefit of eddy currents being independent of the subject scanned is that the affine warp used in the correction can be obtained by imaging a physical phantom with known ground truth [44]. This warp can then be applied to later subject scans.

1.3.2 Subject Motion

Depending on the number of diffusion weighted images being acquired, the length of a diffusion MRI scan can range from a couple of minutes [88] to a few hours [119]. During that time, the subject may move both voluntarily or involuntarily (*e.g.,* breathing). As a result, the same voxel location in two diffusion weighted images is not guaranteed to correspond to the same anatomical location in the subject.

While correcting for subject motion in a single image has been well studied (see [114] for a survey), the problem of correcting motion between separate diffusion weighted images has yet to receive a strong theoretical treatment [14]. Even so, two main approaches have been proposed to correct for subject motion between diffusion weighted images, both involving image registration. First, we can, as with eddy current correction, align the diffusion weighted images to a T_2 weighted image with the mutual information similarity measure [84, 105]. The alternative approach is to model the diffusion at each voxel (as discussed further in Section 2) and to align images so as to minimize the residual of the model fit [7, 11]. A recent quantitative comparison of these approaches suggests that both methods are equally capable of correcting for subject motion [106].

Note however that if the rotational motion of the subject is large, the directions of the applied gradient pulses would need to be corrected for any further model fitting or analysis [78, 105].

1.3.3 Rician Noise

Any environment is going to contain a certain amount of background noise. In the case of diffusion MRI, this noise has been well modeled using a Rician distribution [17] given as

$$p(x|\mu,\sigma) = \frac{x}{\sigma^2} \exp\left(-\frac{x^2+\mu^2}{2\sigma^2}\right) I_0\left(\frac{x\mu}{\sigma^2}\right) \tag{3}$$

where x is the observed image intensity, μ is the noise-free signal, σ is the standard deviation of the noise, and I_0 is the zeroth-order Bessel function of the first kind. At high signal to noise ratios, the Rician distribution is occasionally approximated using a Gaussian distribution [54]. This additive noise can have an adverse effect on the diffusion rates calculated using the Stejskal-Tanner equation, particularly for images taken at a high diffusion weighting [71].

Historically, variational methods have been applied to remove this Rician noise, with anisotropic filtering [99] and total variation regularization [17, 54] both showing success. Weighted mean filtering approaches have also been used [22, 113, 122]. The main conceptual difference in denoising algorithms for diffusion weighted images is whether to denoise one image at a time (the scalar approach) or all images at once (the vector approach) [54]. Recent results suggest that the vector-based algorithms improve signal-to-noise ratio to a greater extent [113].

2 Modelling Local Diffusion Patterns

Since the introduction of diffusion MRI, two key advancements have propelled the field to where it is today: first, the introduction of the diffusion tensor by Basser et al. [15] and second, the introduction of higher angular resolution diffusion imaging (HARDI) [116]. The introduction of the diffusion tensor brought forth the concept of modeling the diffusion rates from the DWIs as a three dimensional function within each voxel. HARDI, on the other hand, allowed us to increase the complexity of these models to better represent the local diffusion properties. This section will show how these two contributions underlie the ability to perform brain connectivity analysis.

2.1 The Diffusion Tensor Model

While the Stejskal-Tanner equation (2) relates diffusion rates to the diffusion weighted image intensities, we can consider a more general formulation of the diffusion properties at a voxel. Since water molecules undergo random Brownian motion, we can consider a probability density function (PDF) $p_t(\mathbf{x})$ describing the probability of a water molecule experiencing a displacement $\mathbf{x}$ over the observation time t. It has been shown that the distribution p_t is related to the diffusion weighted image intensities via the Fourier transform [5]:

$$\frac{S(\mathbf{g})}{S_0} = \int_{\mathbf{x}\in\mathbb{R}^3} p_t(\mathbf{x}) \exp\left(-ib\mathbf{g}\mathbf{x}\right) d\mathbf{x} \tag{4}$$

As earlier, $S(\mathbf{g})$ represents the diffusion weighted signal for the gradient direction $\mathbf{g}$, S_0 is the unweighted $B0$ image signal, and b is the diffusion weighting. With enough diffusion weighted images $S(\mathbf{g})$, the Fourier transform can be inverted to obtain p_t. This is known as *q-space* imaging [119]. In practice however, the number of diffusion weighted images required to accurately perform the inversion leads to scanning times on the order of hours [64] which is generally not available in a clinical setting. As a result, it has become common to assume a model for p_t, the simplest model being a zero-mean Gaussian:

$$p_t(\mathbf{x}) = \frac{1}{\sqrt{(2\pi)^3|2t\mathbf{D}|}} \exp\left(\frac{-\mathbf{x}^T\mathbf{D}^{-1}\mathbf{x}}{4t}\right) \tag{5}$$

where the covariance is $2t\mathbf{D}$. Plugging the Fourier transform of (5) into (4) results in a more general case of the Stejskal-Tanner equation:

$$S(\mathbf{g}) = S_0 \exp\left(-b\mathbf{g}^T\mathbf{D}\mathbf{g}\right) \tag{6}$$

The 3x3 second-order positive-definite symmetric matrix $\mathbf{D}$ is referred to as the *diffusion tensor* [15]. It contains six unique elements and therefore six diffusion weighted images are required, along with the $B0$ image, to estimate the tensor. The diffusion weighted images are obtained from uniform, non-colinear gradient directions so as to not favor a given direction in the tensor fitting process. These seven images can be obtained with an MRI scan on the order of 1-2 minutes [88], thereby making it a clinically feasible imaging protocol.

Many factors affect the quality of the diffusion tensors. As mentioned earlier, noise, motion, and distortions in the diffusion weighted images will result in poor tensor estimates. Aside from

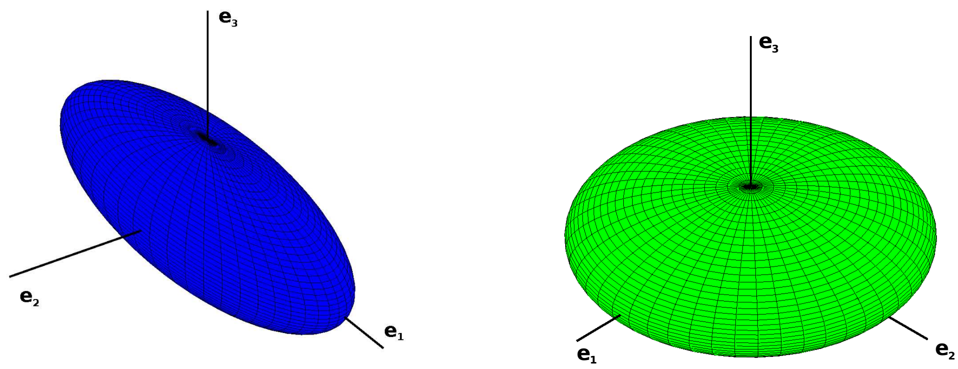

Figure 5: Examples of the ellipsoidal representation of prolate (a) and oblate (b) diffusion tensors. Adapted from [69].

post-processing the diffusion weighted images, it is also common to obtain DWIs from more than six gradient directions in order to overfit the tensor, thereby reducing the effect of having some corrupted DWI signals [71]. The fitting procedure also affects the quality of the resulting tensors. The simplest approach is to take the logarithm of (6) and fit the tensor using least squares [15]. This approach, however, does not ensure that the resulting tensor is positive-definite (*i.e.,* have positive eigenvalues). Non-linear fitting allows for this constraint and generally results in a less noisy tensor field [71], especially if spatial regularization is incorporated into the fitting procedure [118]. Additional approaches include using a weighted least squares fitting of the log-transformed equation (6) which is used to detect and remove outlier DWI signals prior to the final tensor fit [43].

2.2 Tensor Image Visualization

The power of the diffusion tensor lies in its ability to capture and visualize more detailed properties of the diffusion than the scalar diffusion weighted images provide. For example, we can look at how the rates of diffusion vary with direction or calculate the average diffusion rate at each voxel. In fact, significant diagnostic information can be obtained from the diffusion tensor by analyzing its principal components obtained through the tensor's eigendecomposition [61]. Given a diffusion tensor $\mathbf{D}$, we can obtain the eigendecomposition

$$\mathbf{D} = [\mathbf{e}_1 \quad \mathbf{e}_2 \quad \mathbf{e}_3] \begin{bmatrix} \lambda_1 & & \\ & \lambda_2 & \\ & & \lambda_3 \end{bmatrix} [\mathbf{e}_1 \quad \mathbf{e}_2 \quad \mathbf{e}_3]^T \tag{7}$$

where the eigenvalues are positive and sorted in descending order (*i.e.,* $\lambda_1 \geq \lambda_2 \geq \lambda_3$). The eigenvectors $\mathbf{e}_1, \mathbf{e}_2, \mathbf{e}_3$ are considered the main axes of diffusion while the eigenvalues encode the rates of diffusion along each corresponding axis. Given this interpretation, we can visualize the diffusion tensor as an ellipsoid as shown in Figure 5. The axes of the ellipsoid are the eigenvectors of the tensor while the tensor's eigenvalues describe the ellipsoid's stretch along each axis. Another interpretation of the ellipsoid is as an iso-probability surface of the Gaussian diffusion model given in (5).

The tensor eigendecomposition allows for the computation of two key diffusion properties: the Mean Diffusivity (MD) and the Fractional Anisotropy (FA) [69, 120]. These two measures respectively capture the mean and variance of the diffusion rate with respect to direction. They are computed from the tensor's eigenvalues as

$$MD = \frac{1}{3}\left(\lambda_1 + \lambda_2 + \lambda_3\right) \tag{8}$$

$$FA = \sqrt{\frac{3}{2}}\frac{\sqrt{(\lambda_1 - MD)^2 + (\lambda_2 - MD)^2 + (\lambda_3 - MD)^2}}{\sqrt{\lambda_1^2 + \lambda_2^2 + \lambda_3^2}} \tag{9}$$

Examples of MD and FA on a slice of the brain are shown in Figure 6. From these images, we observe the brain microstructure described in Section 1.1. Note that the mean diffusivity is higher in the ventricles than the rest of the brain due to the lack of tissue structure. Conversely, the fractional anisotropy is highest in the white matter of the brain due to coherent orientation of the tissue fibers. We can further estimate the orientation of this microstructure as being equivalent to $\mathbf{e}_1$. Of course, the quality of this estimate will depend in part on the FA. Low fractional anisotropy would imply a less coherent orientation in the tissue fibers, making this estimation of the fiber orientation a potentially poor one.

Other scalar measures have been generated to characterize both the shape and anisotropy of diffusion tensors, but FA and MD are most commonly used in practice. A review of other scalar tensor measures can be found in [90, 120].

Aside from visualizing the scalar FA and MD maps, approaches have been developed to display the tensor's orientation information as well. The two most common approaches are shown in Figure 6. First, the primary diffusion direction $\mathbf{e}_1$ can be visualized as a color image, where the RGB values are $R = FA|\mathbf{e}_1 \cdot [1,0,0]|$, $G = FA|\mathbf{e}_1 \cdot [0,1,0]|$, and $B = FA|\mathbf{e}_1 \cdot [0,0,1]|$ [96]. Such a scheme allows for an intuitive visualization of fiber orientation weighted by the the reliability of that estimate, yet color assignments are not unique. For example, the color yellow would be assigned to voxels with $\mathbf{e}_1 = [1,1,0]$ and $\mathbf{e}_1 = [-1,1,0]$, leading to ambiguity of the underlying fiber direction. As a result, it is occasionally necessary to visualize the tensor ellipsoids themselves as seen in Figure 6(b). Note that generating color representations of tensor data remains an area of open research [60].

Regardless of the visualization strategy, the value of the orientation information in Diffusion MRI is significant as it allows us to infer the orientation of neural pathways in the white matter of the brain. If we take, for example, the color-coded orientation map in Figure 6, we can see four major neural pathways. The genu of the corpus callosum can be seen in red in the upper portion of the image and arching upwards in a U-shape. A similar looking pathway, the splenium of the corpus callosum, can be seen in the bottom half of the image flanked on each side by the optic radiations in green. Finally, the corticospinal tract, which connects the spinal cord to the motor cortex, can be seen in blue (coming out of the page) in the middle of the brain. These pathways, as seen in diffusion MRI, agree with histological studies [41], thereby making diffusion MRI a powerful tool for mapping out these neural pathways non-invasively.

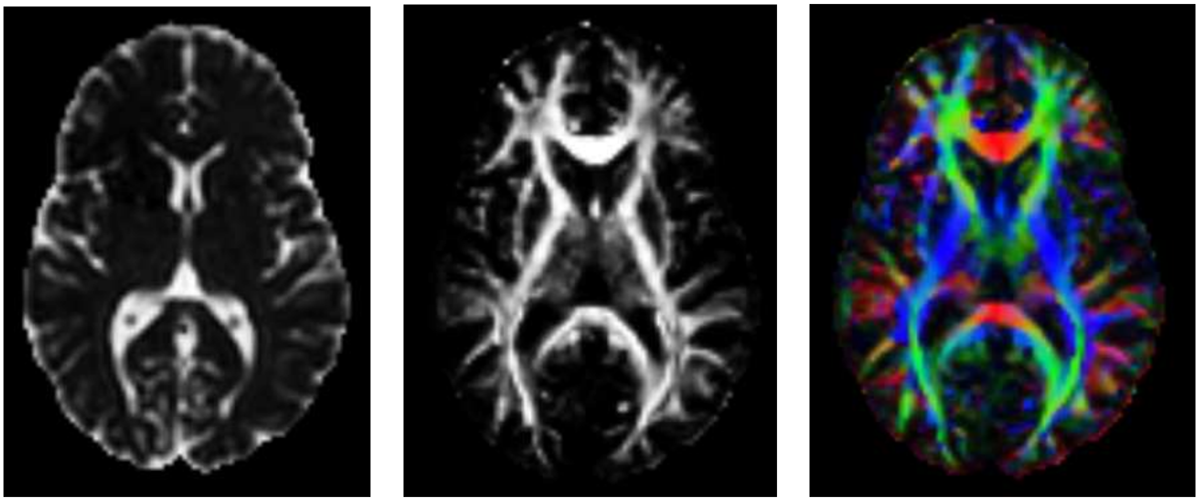

(a) Mean Diffusivity (left), Fractional Anisotropy (center), and Color-coded Orientation Map (right)

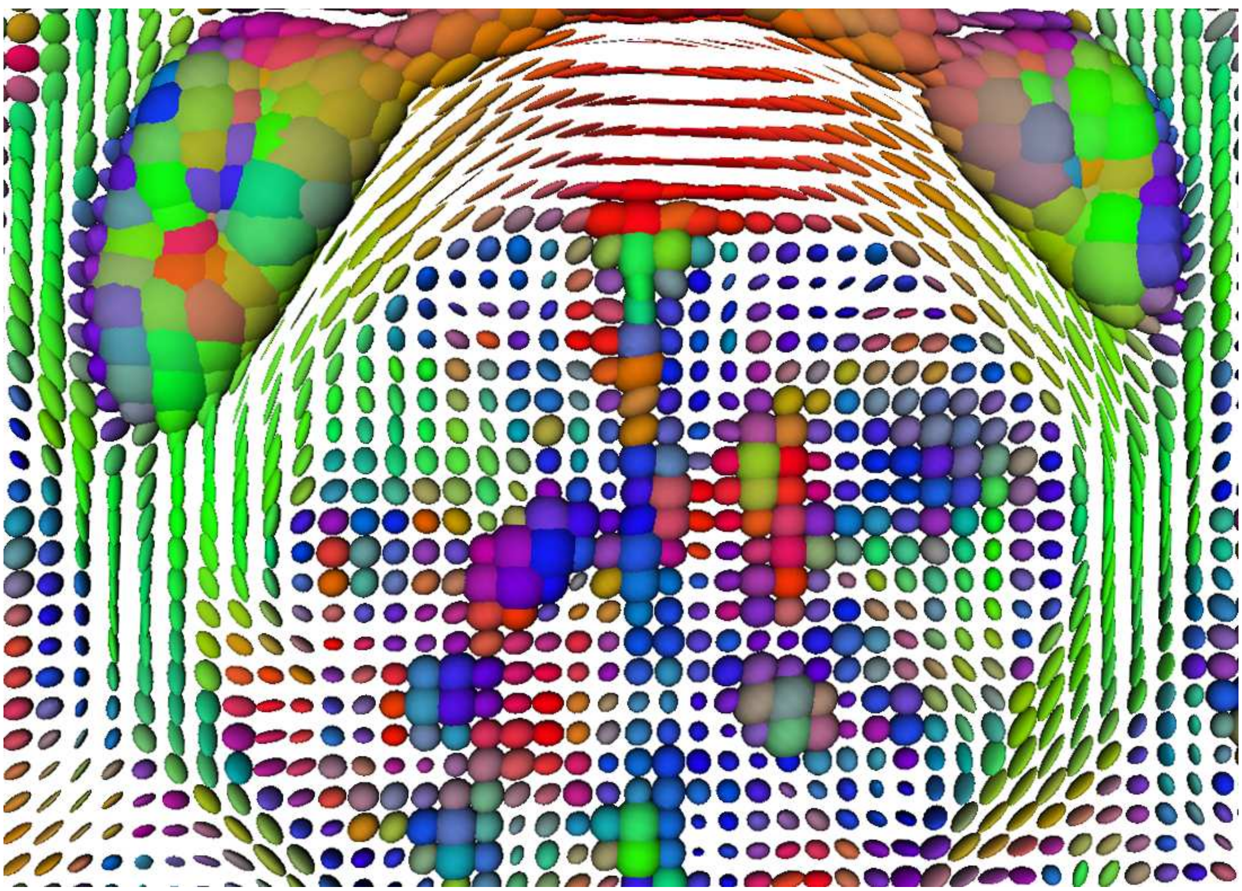

(b) Ellipsoidal Visualization

Figure 6: Various methods of visualizing the information contained in a diffusion tensor field. Images generated using MedINRIA (http://www-sop.inria.fr/asclepios/software/MedINRIA/) on data obtained from [85].

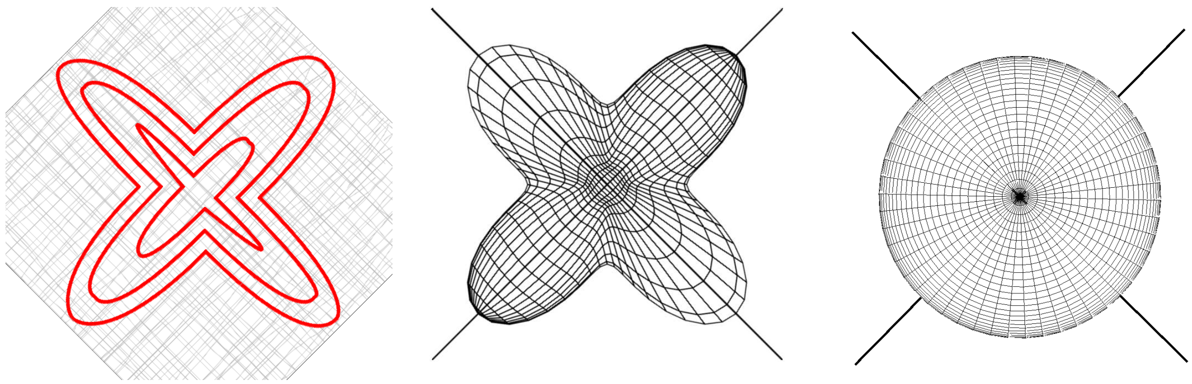

(a) Crossing Fibers (b) Corresponding Diffusion ODF (c) Corresponding Diffusion Tensor

Figure 7: Example of crossing fibers and how they are modeled using Diffusion MRI. Adapted from [4, 48, 120] respectively.

2.3 High Angular Resolution Diffusion Models

While the diffusion tensor model provides a powerful tool for visualizing and assessing the microstructure of brain tissue, it suffers from a significant limitation: the assumption that diffusion follows a Gaussian model. While this model may hold for simple examples such as those in Figure 1, there exist many situations where the local diffusion is more complex.

Take for example, this situation shown in Figure 7(a). This example shows a mixture of fibrous tissues oriented along the positive and negative diagonal directions, resulting in a diffusion profile in red. Ideally, we would like to model this diffusion as shown in Figure 7(b). Unfortunately, the diffusion tensor model assumes ellipsoidal Gaussian diffusion. As a result, we would obtain for this example the tensor shown in Figure 7(c). This tensor would misleadingly suggest that diffusion is equal for all directions in the plane of the crossing. Further, the primary eigenvector of the tensor is not guaranteed to align with either fiber direction.

Such an example is common in the white matter of the brain. The neural pathways are made up of aligned tissue fibers whose diameter is on the order of microns [3]. In contrast, the resolution of diffusion weighted images is typically on the order of millimeters cubed. As a result, this type of averaging of diffusion from multiple pathways is unavoidable. In fact, it has been estimated that at least one third [23] to two thirds [48] of voxels in the brain may exhibit this crossing fiber property.

Tuch et al. first proposed the use of more descriptive diffusion models by showing that there are regions in the brain where fiber cross [116]. They noted that in order to detect these crossing fibers, diffusion weighted images from a greater number of diffusion directions, and at a higher gradient weighting, were required. Thus was born the concept of Higher Angular Resolution Diffusion Imaging (HARDI).

Various attempts have been made to come up with HARDI models that can describe multiple fiber populations at a single voxel. While work has been done in reviewing and comparing these different HARDI approaches [4, 3, 2, 102], there is generally no consensus as to which HARDI model is best suited to represent diffusion MR characteristics. While research in this area is ongoing, three main classes of HARDI models have established themselves. We examine each in turn.

2.3.1 Compartment Models

Initial attempts to model more complicated diffusion profiles revolved around fitting multiple tensors to the different fiber populations (*i.e.,* compartments) of the diffusion weighted image signals [116]. A mixture of Gaussians model is commonly assumed and the Stejskal-Tanner equation was updated to incorporate the mixture.

$$\frac{S(\mathbf{g})}{S_0} = \sum_i f_i \exp\left(-b\mathbf{g}^T \mathbf{D}_i \mathbf{g}\right) \tag{10}$$

Each tensor $\mathbf{D}_i$ has a corresponding volume fraction f_i representing the fraction of the local diffusion the fiber population represents. Later work using the CHARMED [9, 8] and FORECAST [6] methods assumed a particular shape for each fitted tensor. The former approach attempts to model intra-fiber and extra-fiber diffusion using prolate (cigar-like) and spherical tensors respectively. The latter approach models prolate tensors with an equal and known mean diffusivity. More recent work has instead assumed a mixture of Wishart (MOW) distributions - effectively a distribution over tensors - as the choice of diffusion model [68, 67]. A recent and thorough review of these compartment models can be found in [97].

While these mixture model approaches allow for the same intuitive representation as the single tensor model, they also have their limitations. These include:

- The number of tensors being fitted to the DWI signal has to be specified ahead of time. While there has been work on estimating this number from the data [5, 116], there is no ground truth specification for the number of tensors to fit at a voxel.
- There is no guarantee that the assumed shape of the fitted tensors is appropriate for the underlying diffusion. If the shape assumption is poor, the volume fractions can be poorly estimated [6].
- The mixture model, and not the underlying mixture components, is fit to the DWIs. While the peaks of the mixture model will align with the directions of maximal diffusion, there is no guarantee that the peaks of the underlying distributions will align with these directions as well [116, 117].

Some of these limitations have been addressed in recent work. For example, instead of fitting a fixed number of tensors to the data, volume fractions can be calculated for a set of basis tensors [81, 68, 67]. Those tensors with a volume fraction above a given threshold are maintained to model the diffusion.

2.3.2 Higher Order Tensors

While compartment models increase the fidelity of the tensor fitting by mixing multiple, simple tensor models, it is also possible to increase the complexity of the tensor model itself [12, 49, 82, 93]. By introducing a higher-order tensor representation into the Stejskal-Tanner equation, we obtain

$$\frac{S(\mathbf{g})}{S_0} = \exp\left(-b\sum_{i_1=1}^{3}\cdots\sum_{i_\ell=1}^{3}\mathbf{D}_{i_1\cdots i_\ell}\mathbf{g}_{i_1}\cdots\mathbf{g}_{i_\ell}\right) \tag{11}$$

where the ℓ-th order tensor $\mathbf{D}$ represents an ℓ-dimensional grid of entries and has the degrees of freedom necessary to model non-Gaussian diffusion [93, 82]. Note that by moving to this higher-dimensional representation, we no longer make a Gaussian assumption on the diffusion PDF. Instead, the higher-order tensor captures higher-order moments of the diffusion signal [12]. One such example of modeling these higher-order moments is in Diffusion Kurtosis Imaging, where the diffusion PDF is modeled using both a regular diffusion tensor for the Gaussian part of the diffusion PDF and a 4th order tensor for the kurtosis of the diffusion PDF [65].

Like ordinary diffusion tensors, various diffusion features can be extracted from a higher order tensor. The majority of these features are based on the higher order tensor's directional profile

$$D(\mathbf{g}) = \sum_{i_1=1}^{3}\cdots\sum_{i_\ell=1}^{3}\mathbf{D}_{i_1\cdots i_\ell}\mathbf{g}_{\measuredangle i_1}\cdots\mathbf{g}_{\measuredangle i_\ell} \tag{12}$$

where $D(\mathbf{g})$ is the diffusion rate along unit direction $\mathbf{g}$ and $\mathbf{g}_{\measuredangle i_j}$ is the vector $\mathbf{g}$ projected onto the i_j-th axis of the higher order tensor. From this directional profile, we can obtain features equivalent to mean diffusion and fractional anisotropy by taking, respectively, the mean and variance of $D(\mathbf{g})$ [93]. A recent review of higher order tensors is available in [12].

Unlike compartment models, higher order tensors have the benefit of modeling non-Gaussian diffusion without having to specify the number of fiber compartments present. However, there persists the concern that the maxima of (12) are not guaranteed to line up with the underlying fiber tract directions [117].

2.3.3 Diffusion Orientation Distribution Functions

On the other end of the spectrum, model-free approaches have also been proposed to capture local diffusion properties. Again, Tuch instituted this approach through the introduction of *q-ball* imaging [115]. Based on the earlier *q-space* approach described by the Fourier transform in (4), Tuch noticed that the directional dependence of the diffusion rate is the most commonly used information for diffusion MRI analysis and that the radial distance component of the diffusion does not play a significant role. As a result, instead of modeling the diffusion as a PDF $p(\mathbf{x})$, where $\mathbf{x}$ is a vector of any length, *q-ball* imaging models the diffusion orientation distribution function (ODF) $\psi(\theta, \phi)$, where θ, ϕ are spherical angles. As such, the ODF captures the probability of diffusion along different angular directions (θ, ϕ) but without a radial distance parameter. An estimation of the ODF can be more efficiently obtained through the use of the Funk-Radon transform [115]. By ignoring the radial component, the *q-ball* ODF can be estimated with fewer diffusion weighted image samples than the original PDF from *q-space* imaging, leading to more reasonable scanning times.

Other model-free approaches have also gained traction in the diffusion MRI community. First, the diffusion orientation transform (DOT) shares similarities with *q-ball* imaging as both are based on the earlier *q-space* approach. In contrast, DOT assumes diffusion is Gaussian along the radial direction and uses this assumption to perform the Fourier transform in (4) using fewer diffusion weighted image samples [95]. The DOT diffusion ODF is then obtained by analytically integrating the resulting PDF along the radial direction.

An alternative model-free approach is Jansons and Alexander's Persistent Angular Structure (PAS) approach [64]. The goal behind PAS is to find a diffusion PDF $p(\mathbf{x})$ from (4) that is both smooth yet captures the key angular structure of the diffusion. This goal is achieved through optimization by finding a PDF $p(\mathbf{x})$ that maximizes entropy while minimizing the error in fitting to the diffusion weighted image samples. A Lagrange multiplier is used to weight the two competing terms [64].

Unlike the diffusion tensor, the diffusion ODF is a spherical function that can be represented in many ways [66, 103]. The most popular choice for its representation is a real spherical harmonic expansion [6, 50, 66]. The diffusion ODF ψ can be represented as:

$$\psi(\theta, \phi) = \sum_{\ell=0}^{K} \sum_{m=-\ell}^{\ell} F_\ell^m Y_\ell^m(\theta, \phi) \tag{13}$$

where integers ℓ and m are the degree and order of the harmonics respectively. The basis harmonics Y_ℓ^m are given as:

$$Y_\ell^m = \begin{cases} \sqrt{\frac{2\ell+1}{4\pi}} P_\ell^0(cos(\phi)), & \text{if } m = 0 \\ \sqrt{2}\sqrt{\frac{2\ell+1}{4\pi}\frac{(\ell-m)!}{(\ell+m)!}} P_\ell^m(cos(\phi))cos(m\theta), & \text{if } m > 0 \\ \sqrt{2}\sqrt{\frac{2\ell+1}{4\pi}\frac{(\ell-m)!}{(\ell+m)!}} P_\ell^{-m}(cos(\phi))sin(m\theta), & \text{if } m < 0 \end{cases} \tag{14}$$

where P_ℓ^m is the associated Legendre function of degree ℓ and order m. As the ODF is anti-podally symmetric, only the even degree basis harmonics are used [50]. Typically, the expansion is limited to degree $\ell \leq 8$ to suppress noise artifacts in the resulting ODF [48]. Other ODF representations have also seen limited use, including von Mises-Fisher and Watson distributions [103].

The notions of mean diffusivity and fractional anisotropy have also been extended to HARDI diffusion ODFs, with the latter being referred to in this context as generalized anisotropy (GA). Similar to the tensor case, the two measures correspond to the mean and variance of the diffusion ODF ψ:

$$MD = \frac{1}{4\pi} \int \psi(\theta, \phi) dS \qquad GA = \frac{1}{4\pi} \int \left(\psi(\theta, \phi) - MD\right)^2 dS \tag{15}$$

Unlike the diffusion tensor model, MD and GA generally do not have an elegant solution. Analytical solutions have been proposed for both measures [94] but involve ad hoc scaling and normalization weights. Examples of MD and GA images are shown in Figure 8. We can also visualize the orientation information in the diffusion ODF by visualizing the spherical functions themselves as seen in Figure 8.

Various other model-free diffusion ODF estimation procedures have been recently proposed and a thorough review of these techniques is available in [10]. One of the key limitations of the model-free HARDI approaches is precisely that a model is not assumed. In areas of low anisotropy, both PAS and *q-ball* imaging can overestimate the directional dependence of the diffusion as a result of image noise [64, 115]. This overestimation can result in spurious maxima in the diffusion ODFs.

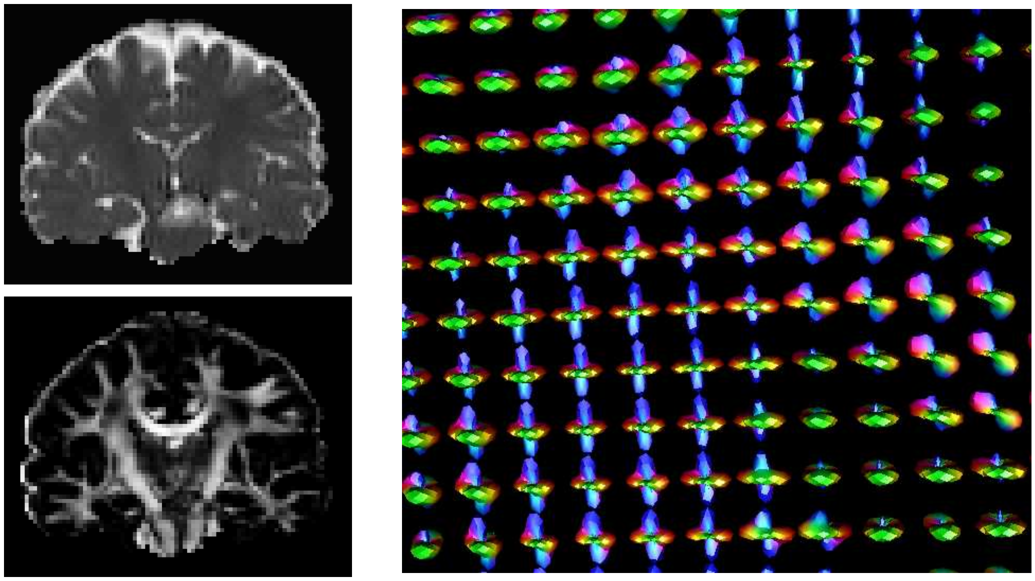

(a) Mean Diffusivity (top) and Generalized Anisotropy (bottom)

(b) *q-ball* Diffusion ODFs

Figure 8: Sample visualization techniques for diffusion ODFs obtained from HARDI.

2.4 HARDI versus the Diffusion Tensor

Despite the presence of these HARDI models that better represent the underlying diffusion properties, the use of the diffusion tensor model still persists in a clinical setting [88, 89, 91]. There are various reasons for the use of what is perceived to be an inferior model and these reasons highlight some of the limitations of HARDI:

- The number of gradient directions, and in turn diffusion weighted images, required for the reconstruction of HARDI models is still significantly larger than for diffusion tensor imaging. With scanning time as a bottleneck, the opportunity to obtain enough diffusion weighted images for a HARDI reconstruction remains, in many cases, a luxury.

- To observe non-Gaussian diffusion, the strength of the magnetic gradients used in the scan is increased [116]. Increasing the gradient strength increases diffusion rates, which in turn are inversely proportional to relaxation time and diffusion weighted image intensity. If we increase the gradient strength enough, the diffusion weighted image intensities can fall below the noise floor, an effect seen with HARDI imaging settings [71].

- Recent research suggests that limitations of the tensor model with regards to crossing fibers might be overcome by taking into account neighborhood information [13, 107]. With such advancements, it remains unclear at this time if HARDI can provide enough additional information over a diffusion tensor image to warrant the added imaging cost.

Due to these above reasons, and the wealth of diffusion tensor medical research [91], the tensor model cannot be ignored.

3 Brain Connectivity Mapping from dMRI

The orientation information in diffusion MRI is incredibly valuable in mapping out neural pathways in the white matter of the brain. As diffusion is strongest along the fiber tracts that make up neural pathways, the directions of maximal diffusion at each voxel location can be used to help reconstruct the fiber tracts, thereby mapping out connectivity in the brain. The problem of mapping out these connections is known as tractography and is complicated by many factors. We have already mentioned two: poor diffusion model fitting and noisy diffusion measurements. Here, we look at how these complications, and others, have led to the development and evolution of various tractography algorithms.

3.1 Streamline Tractography

The earliest approaches to the tractography problem surrounded tracing out 3D curves that followed the direction of strongest diffusion [16, 86]. These 3D curves, known as streamlines, evolve using the following Euler equation:

$$\mathbf{r}(s_{i+1}) = \mathbf{r}(s_i) + \alpha\varepsilon_1(\mathbf{r}(s_i)) \tag{16}$$

where $\mathbf{r}$ is the streamline curve parametrized by its length from a given seed point, and s_i are points along the curve. ε_1 is the primary diffusion direction (PDD) at the given location on the curve and the choice of notation comes from the use of the diffusion tensor's primary eigenvector as the PDD. The PDD acts as the tangent to the streamline as it evolves with stepsize α, where α is sufficiently smaller than the voxel size to limit discretization effects on the evolving curve. These aspects are further shown in Figure 9. While the above Euler equation most easily describes the streamline evolution, a higher-order Runge-Kutta method is commonly used to improve numerical stability in the streamline evolution [16]. The streamline evolution continues until the PDD becomes unreliable. Typically, the reliability of the PDD is captured through either fractional anisotropy [16] or via neighborhood PDD coherence [86]. This initial tractography approach is referred to in the literature as the *fiber assignment by continuous tracking* (FACT) method.

One of the concerns with the FACT approach is that it follows the PDD regardless of whether the PDD at a voxel is an accurate estimation of fiber tract orientation. In areas of lower anisotropy (but still above the termination threshold of FACT), the PDD may become more unreliable. In these situations, we may wish to regulate the effect of the local PDD on the direction of the evolving streamline. This is the idea behind the tensor deflection (TEND) approach [77]. In this algorithm, the local diffusion tensor $\mathbf{D}$ is used to deflect the incoming streamline curve as given by the evolution equation:

$$\mathbf{r}(s_{i+1}) = \mathbf{r}(s_i) + \alpha\mathbf{D}(\mathbf{r}(s_i)) \cdot \mathbf{r}(s_i) \tag{17}$$

The greater the anisotropy of the tensor, the more reliable the PDD and therefore the stronger the deflection of the streamline fiber. An example of this evolution is shown in Figure 9(c).

By deflecting the incoming streamline curve, TEND implicitly creates a curvature constraint on the evolving streamline. The streamline can only bend as much as a diffusion tensor will allow. In some situations, this curvature constraint can cause the TEND algorithm to deviate from

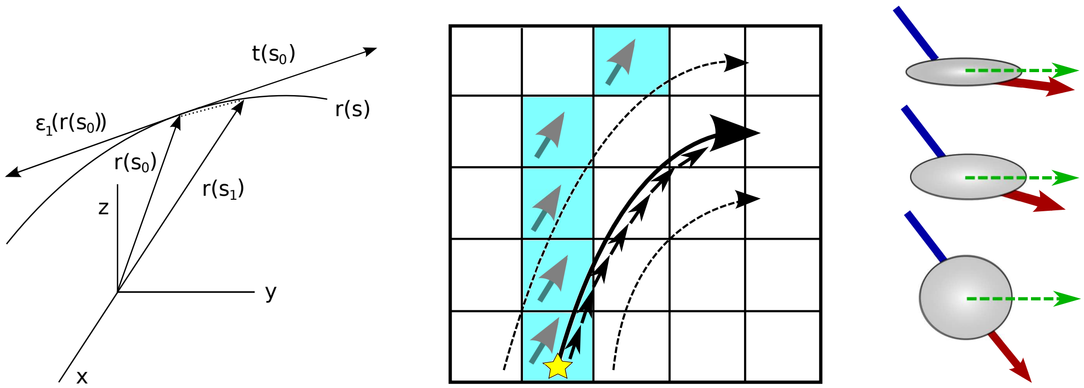

(a) Streamline tangent to PDD (b) Effect of stepsize on streamline tractography (c) Tensor Deflection

Figure 9: Examples of streamline evolution. Streamlines evolve in the direction tangent to the local primary diffusion direction. Step sizes in the evolution equation are chosen sufficiently small so as to avoid poor tracking due to discretization. Adapted from [16, 86, 77] respectively.

a high curvature fiber tract, thereby generating a poor result [46]. To compensate for this effect, the tensorline approach was proposed [77] that evolves the streamline curve based on a weighted combination of (16) and (17). As a result, the curvature can be turned on and off based on local anisotropy or prior knowledge. Streamline tractography has also been extended to compartment models [25] and diffusion ODFs using extracted ODF maxima [28]. In these cases, streamlines follow the PDD that creates a minimal angle with the incoming curve. A further review can be found in [125].

From a computational standpoint, these streamline approaches have many limitations, namely

- Streamline approaches only follow one tract at a time. The algorithm cannot naturally handle situations where tracts fan out or cross. One approach to address this concern is to perform a brute force implementation of the algorithm where every point of the brain is, in turn, used as a seed. The tracts that are kept are ones that flow through one or more regions of interest [87]. Even so, this brute force approach doesn't guarantee that crossing or kissing (*i.e.,* barely touching) fibers are appropriately handled.

- These algorithms, particularly the FACT algorithm, assume that the principal diffusion direction is an accurate and error-free estimate of the fiber direction. Any error in the PDD measurement propagates to the streamline curve, and that error will accumulate with each step taken. Error in the PDD, while small at each step, can accumulate to the point where the streamline can "jump" into a neighboring tract, thereby giving a false display of anatomical connectivity [87].

- Despite the above issues, these tractography algorithms present a binary result: a 3D space curve. There is no representation of the confidence or accuracy of the resulting streamline tract. Attempts are being made to quantify tract confidence from streamlines [36, 37], but addressing this problem is still in the early stages.

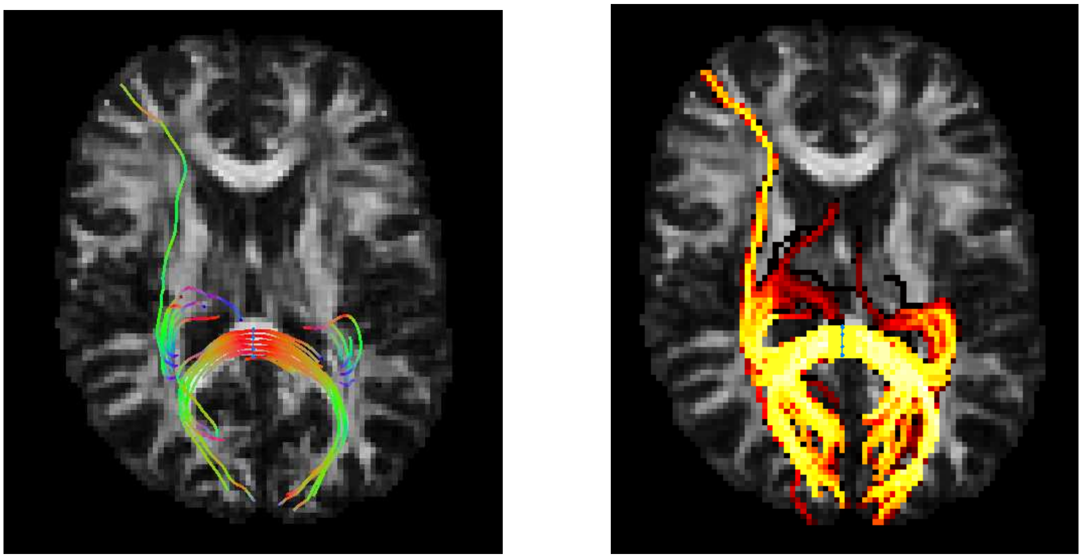

(a) Streamline Tractography (b) Probabilistic Tractography

Figure 10: Examples of streamline and probabilistic tractography applied to a seed region in the Splenium of the Corpus Callosum. Note that since probabilistic tractography uses streamline tractography as an underlying mechanism, the results are similar.

Even so, streamline tractography has been successful in detecting major fiber tracts like the Forceps Major shown in Figure 10(a).

3.2 Probabilistic Tractography

One of the major concerns with streamline tractography was the amount of confidence we can have in the accuracy of the generated tracts. This concern has led to significant work in trying to perform tractography from a probabilistic point of view. Given points A and B in a diffusion MR image $\mathcal{I}$, probabilistic tractography algorithms attempt to compute the probability of a tract connecting A and B. Formally, that probability is given as:

$$p(A \to B|\mathcal{I}) = \sum_{n=1}^{\infty} \int_{\Omega^n_{AB}} p(n)p(\mathbf{v}_{1:n}|\mathcal{I})d\Omega^n_{AB} \tag{18}$$

where n is the length of the tract, $\mathbf{v}_{1:n}$ is a random path of length n, and Ω^n_{AB} is the space of fiber tracts of length n that connect A to B [53]. Given the exponential number of paths in the space Ω^n_{AB}, this integration cannot be done analytically. Instead, the probability $p(A \to B|\mathcal{I})$ is sampled through the use of Markov Chain Monte Carlo (MCMC) [74, 53, 24, 27].

Conceptually, MCMC-based probabilistic tractography shares many similarities with streamline tractography algorithms. Both trace out 3D streamlines by following a local tangent vector. The differences with probabilistic tractography approaches is that instead of exclusively using the principal diffusion direction as the local tangent to the curve, they sample each tangent vector $\mathbf{v}_i$ from a given distribution $p_i(\mathbf{v}_i|\mathbf{v}_{i-1}, \mathcal{I})$. Also, hey repeat the streamline tractography many times from the same seed A. Each resulting streamline is considered a sample of $p(A \to B|\mathcal{I})$. With enough of these samples (K), we can obtain a reasonable approximation of the probability that regions A and B are connected:

$$p(A \to B|\mathcal{I}) = \sum_{n=1}^{\infty} \sum_{k=1}^{K} p(n) \frac{\vartheta(\mathbf{v}_{1:n}^{k})}{K} \tag{19}$$

The function $\vartheta(\mathbf{v}_{1:n}^{k})$ is equal to one if path k connects regions A and B and zero otherwise. The prior probability $p(n)$ is usually taken to be uniform, thereby being unbiased to path length. Effectively, the probability that A and B are connected is equal to the fraction of random paths that connect A and B [27]. Probability maps containing the values from (19) can then be displayed and analyzed. An examples is shown in Figure 10(b).

While many probabilistic tractography algorithms have been proposed, their key differences seem to lie in how the distribution $p_i(\mathbf{v}_i|\mathbf{v}_{i-1}, \mathcal{I})$ models the local tangent vectors $\mathbf{v}_i$ that make up each random path. This tangent vector distribution is commonly split into two independent terms

$$p_i(\mathbf{v}_i|\mathbf{v}_{i-1}, \mathcal{I}) = p_i(\mathbf{v}_i|\mathcal{I})p(\mathbf{v}_i|\mathbf{v}_{i-1}) \tag{20}$$

where the first distribution, $p_i(\mathbf{v}_i|\mathcal{I})$ captures the likelihood of a fiber direction given the image data, while the second distribution, $p(\mathbf{v}_i|\mathbf{v}_{i-1})$ imposes a smoothness constraint. The smoothness constraint is typically represented by a Bernoulli distribution with $p(\mathbf{v}_i|\mathbf{v}_{i-1}) = 1$ if the angle between $\mathbf{v}_i$ and $\mathbf{v}_{i-1}$ is less than ninety degrees (and zero otherwise). Meanwhile, the image-dependent distribution, known by the name *fiber orientation distribution* (FOD), has received a greater amount of attention. We examine some popular choices for FODs below.

3.2.1 Fiber Orientation Distributions

Fiber orientation distributions are similar in many ways to the diffusion ODFs introduced in Section 2.3. Both are spherical distributions whose maxima are likely directions tangent to fiber tracts. However, FODs capture the likelihood of a fiber tract being tangent to a given direction instead of the likelihood of diffusing along a given direction. Directions with slow diffusion rates in an ODF will still have a non-zero probability, despite that slow diffusion being evidence of no neural connectivity. An FOD, however, will have zero probability for those directions, leading to a sharper probability distribution.

Many techniques have been proposed for computing an FOD and generating a accurate FOD remains an area of open research. Below are the most popular approaches:

Diffusion Profile: We noted earlier that the diffusion tensor describes a Gaussian model of diffusion. As such, this Gaussian model is commonly used as an FOD by integrating along the radial dimension [59, 74]. These Gaussian approaches typically replace the diffusion tensor $\mathbf{D}$ with a scaled version $\mathbf{D}^{\alpha}$ to make the distribution sharper. Sample values for α range from 2 [59] to 7 [74].

HARDI versions have also followed a similar approach with a sharpened version of the diffusion ODF used as an FOD [48, 73].

Heuristic Approaches: Parker et al. proposed the probabilistic index of connectivity (PICo) approach where the FOD is an heuristic distribution based on local anisotropy [98]. The PDD is taken as the mean tangent direction with a cone of uncertainty whose apex angle is a function of a local anisotropy measure.

Bayesian Formulations: The tangent vector distribution can also be described using Bayes rule with respect to the diffusion data:

$$p_i(\mathbf{v}_i|\mathcal{I}) = \frac{p(\mathcal{I}|\mathbf{v}_i)p(\mathbf{v}_i)}{p(\mathcal{I})} \tag{21}$$

The posterior distribution $p(\mathcal{I}|\mathbf{v}_i)$ captures how well the diffusion model fits the diffusion weighted image samples and is typically approximated using a Gaussian distribution on the model's residual fit [24, 23, 45, 53]. The prior on fiber direction, $p(\mathbf{v}_i)$ is typically chosen to be uniform while $p(\mathcal{I})$ can be chosen so as to normalize the distribution.

Statistical Bootstrap: Instead of assuming some distribution for the FOD, some have used bootstrap techniques to approximate the distribution from multiple samples [76, 70, 121]. During the image acquisition process, multiple diffusion weighted images can be obtained for each gradient direction. When it comes to fitting a diffusion model, we can do so by fitting to a randomly selected subset of the DWIs. This fitting process can be repeated for many image subsets, thereby generating multiple diffusion MR images. The distribution of the primary diffusion directions generated from this set of dMRIs can then be used as a model-free approximation of the FOD.

In the absence of multiple DWI acquisitions, wild bootstrap can be performed [70, 121]. In this situation, noise is added to the diffusion weighted images by using random perturbations of the residual of the model fit. The fitting is then re-performed for each set of noise-simulated DWIs to obtain multiple diffusion MR images from which the FOD can be generated.

Unsupervised Learning: In some cases, the diffusion MR data can be used to learn the relationship between the diffusion measurements and the FOD. Tournier et al. proposed the assumption that the voxels of highest FA can be used as examples of voxels where the FOD is a Dirac distribution in the direction of the PDD [111]. Under this assumption, they compute a sparse spherical deconvolution technique that fits a combination of these Dirac FODs to the diffusion weighted data, thereby generating more general FODs.

Probabilistic tractography approaches have the advantage of characterizing uncertainty in the tractography algorithm. Even so, these methods too have their limitations:

- As each step taken along a tract contains some uncertainty, the connection probabilities we obtain using this approach are inevitably linked to the length of the tract. As such, we cannot interpret these probabilities as a measure of tract quality since they are not invariant to length [69].

- As with streamline tractography, noise can still cause the maxima of the tangent vector distribution to be off. There exists no mechanism in the tractography algorithm to correct for this error.

- The number of path samples required to approximate (18) is commonly on the order of thousands [24, 53, 70]. This results in significant computational cost and running times on the order of an hour or more for a given seed point [124]. Some recent work has tried to address this issue through, for example, the use of particle filters [124].

3.3 Front Propagation Tractography

A third set of tractography algorithms can be described as front propagation approaches where some form of information propagates outward from a given seed region at a speed proportional to the amount of fiber tract evidence. The information propagated by the front can then be used to reconstruct the fiber tracts. These algorithms can be divided into three main groups based on their computational aspects.

3.3.1 Fast Marching Tractography

Conceptually, the fast marching tractography approaches are distinguished by the calculation of a time of arrival of the propagating front for each voxel [100]. This arrival time T is related to the speed of the front F via the Eikonal equation

$$|\nabla T|F = 1 \qquad \text{or} \qquad T(\mathbf{r}_i) = T(\mathbf{r}_{i-1}) + \frac{|\mathbf{r}_i - \mathbf{r}_{i-1}|}{F(\mathbf{r}_i)} \tag{22}$$

where $\mathbf{r}_i$ and $\mathbf{r}_{i-1}$ are neighboring voxels on opposite sides of the propagating front. With the arrival times calculated for all voxels, fiber tracts can be delineated by performing gradient descent on the arrival time map. By generating tracts in this fashion, situations of branching and merging fibers are handled naturally through the propagation of the front.

The speed F of the front is set based on the presence or absence of a fiber tract. A common choice is to use the diffusion profile as the speed function [79, 80, 108, 92], thereby ensuring faster speed along directions of faster diffusion. Another choice is neighborhood PDD coherence [100]. By making the front speed an indicator of tract presence, we can characterize the tract's "quality" as some function of the speed. One approach is to characterize the confidence of a tract γ by its weakest link τ [100]:

$$\zeta(\gamma) = \min_{\tau} F(\gamma(\tau)) = \min_{\tau} \frac{1}{|\nabla T(\gamma(\tau))|} \tag{23}$$

While measuring tract quality in this fashion is a heuristic approach, it does provide us with a measure of confidence that is invariant to path length.

3.3.2 Tractography via Flow Simulation

Instead of using an arrival time map for tract reconstruction, we can interleave the two operations, thereby recovering the tract as we propagate the front. Noting that diffusion is fastest along a fiber tract, some researchers [42, 72, 92, 126, 19, 56, 112, 18] have proposed that we simply simulate the diffusion and reconstruct candidate tracts through the analysis of the diffusion front.

The diffusion is simulated using Fick's Second Law [92], given as

$$\frac{\partial u}{\partial t} = \nabla \cdot (\psi \nabla u) \tag{24}$$

where u is the local molecular concentration and ψ is the diffusion function (either the tensor $\mathbf{D}$ [72, 92, 126, 19, 56] or a diffusion ODF in the case of HARDI [42]). Given a seed point, the diffusion process is simulated for a fixed time t. The resulting concentration map u is then

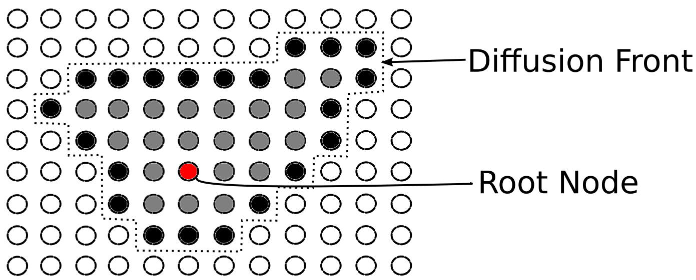

(a) An Example Diffusion Front

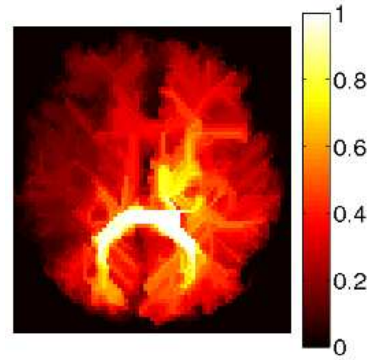

(b) Example of Minimum Path Tractography

Figure 11: Examples of front propagation tractography, specifically the representation of the diffusion front and the connection strengths generated using minimal path tractography on a seed in the Splenium of the Corpus Callosum. Adapted from [72, 31] respectively.

thresholded to obtain the hard diffusion front shown in Figure 11(a). The voxels along the diffusion front can then be scored based on a set of criteria to determine the likelihood that they are on a fiber tract [72, 126, 42]. Sample criteria include distance from the seed point, fractional anisotropy, and path curvature [72]. The diffusion is then simulated at each candidate point and the process repeats itself.

While this approach has generally gone out of favor due to the ad hoc criteria used to select fiber tract points, the ideas generated by this tractography approach have been applied elsewhere. One example is the work of O'Donnell et al. where the steady state flux (*i.e.,* $\frac{\partial u}{\partial t} = 0$) is solved for and fiber curves are computed that maximize the resulting flux [92]. A similar approach is used by Hageman et al. where instead of modeling diffusion, they model fluid flow using the Navier-Stokes equation [58]. By using the fluid flow model, Hageman et al. are capable of adding additional tract information through fluid flow related concepts (*e.g.,* viscosity).

3.3.3 Minimal Path Tractography Algorithms

A third set of tractography algorithms also display this concept of front propagation: graph-based minimal path algorithms [63, 109, 123]. These tractography algorithms discretize the image space into a graph and use Dijkstra's algorithm to obtain the path of strongest diffusion. In this case, the front being propagated is the boundary between the visited and unvisited nodes.

To ensure the shortest path is the path of strongest diffusion, the edge weights in the graph are set to $w(e_{ij}) = -log(P_{diff}(i,j))$, where the pseudo-probability P_{diff} is given as

$$P_{diff}(i,j) = \frac{1}{Z}\left(\int_{(\theta,\phi)\in\beta_i} \psi_i(\theta,\phi)dS + \int_{(\theta,\phi)\in\beta_j} \psi_j(\theta,\phi)dS\right) \tag{25}$$

where ψ_i is the diffusion ODF at voxel i, Z is a normalizing constant, and β_i is the solid angle around the graph edge between i and j [31, 63]. As with the fast marching algorithm, we can consider a "weakest link" connection strength here as well by selecting the largest edge weight along the tract. An example of this form of tractography shown in Figure 11(b).

One must be concerned when using this method to ensure that the angular discretization provided by the edge connectivity is fine enough to avoid diverging effects similar to those in Figure 9.

3.4 Global Tractography

While the tractography algorithms in the previous sections have their conceptual differences, one aspect they do share is that they generate tractography results in a local, greedy fashion. Because of this trait, these tractography algorithms have been prone to amplify localized errors in the data and limit their effectiveness [32, 87]. To address this concern, the field of diffusion MR analysis have been developing techniques that model tractography as a global optimization problem [83].

Generally speaking, global tractography algorithms frame tractography as a curve fitting problem, though how those curves are represented varies. Initial global tractography techniques begin with small, randomly distributed, curve pieces and tries to link them together into fiber tracts that best fit the dMRI data [52, 75]. The optimization is performed globally (*i.e.,* over the whole image space), resulting in algorithms that are more robust to the presence of local difusion measurement errors. More recently, a probabilistic version of this idea was presented by Booth and Hamarneh [32] where graph edges are used in the place of curve pieces. However, the most popular global tractography technique so far has been the Hough transform technique of Ananj et al. [1]. In their technique, a parameterized set of full curves are compared to the dMRI and scored based on how well they explain the image data. Those curves that have the highest scores are chosen to represent axonal tracts.

While these global tractography algorithms generate more robust results than earlier tractography techniques, they are limited by the discretization of the curves they fit to the dMRI data. This discretization has the potential to limit what axonal tracts can be detected and represented with these algorithms. That said, recent work in machine learning may provide the ability to learn a more representative set of discrete curves for these tractography algorithms, which could potentially reduce curve fitting errors [47].

4 Conclusions

Diffusion MRI provides us with the ability to analyze brain connectivity non-invasively. By measuring the diffusion of water molecules along various directions in 3D, and knowing that cell structure restricts molecular diffusion, we are able to infer the directional organization and integrity of fibrous tissue. Further modeling of these diffusion measurements allow us to assess characteristics such as bulk diffusivity and anisotropy. The directional dependence of the diffusion can also be used to trace out the imaged neural fibers.

Various computational aspects of diffusion MRI have been presented in this chapter, from acquiring diffusion-weighted MRI, to modeling the diffusion using diffusion tensors or HARDI models, to uncovering neural pathways with tractography algorithms. These analysis techniques have become even more established with their incorporation into software packages like FSL, MedINRIA, Camino, and TrackVis. These aspects of image analysis merely scratch the surface of what may be possible with this relatively new imaging technique. Already, there is work being done in the areas of segmentation [33, 35, 104], registration [30, 55], and statistics of diffusion MRI data [101]. It is hoped that continued work in diffusion MRI will culminate in the ability to generate a human connectome: a detailed connectivity map of the human brain [38, 40].

References

[1] Iman Aganj, Christophe Lenglet, Neda Jahanshad, Essa Yacoub, Noam Harel, Paul M. Thompson, and Guillermo Sapiro. A hough transform global probabilistic approach to multiple-subject diffusion MRI tractography. *Medical Image Analysis*, 15:414–425, 2011.

[2] D. Alexander. A comparision of q-ball and PASMRI on sparce diffusion MRI data. In *Proceedings of International Society of Magnetic Resonance in Medicine (ISMRM)*, page 90, Kyoto, May 2004.

[3] Daniel C. Alexander. Multiple-fiber reconstruction algorithms for diffusion MRI. *Annals of the New York Academy of Sciences*, 1046:113–133, 2005.

[4] Daniel C. Alexander. *Visualization and Processing of Tensor Fields*, chapter 5: An Introduction to Computational Diffusion MRI: the Diffusion Tensor and Beyond, pages 83–106. Springer Berlin Heidelberg, 2006.

[5] D.C. Alexander, G.J. Barker, and S.R. Arridge. Detection and modeling of non-gaussian apparent diffusion coefficient profiles in human brain data. *Magnetic Resonance in Medicine*, 48:331–340, 2002.

[6] Adam W. Anderson. Measurement of fiber orientation distributions using high angular resolution diffusion imaging. *Magnetic Resonance in Medicine*, 54:1194–1206, 2005.

[7] Jesper L.R. Andersson and Stefan Skare. A model-based method for retrospective correction of geometric distortions in diffusion-weighted EPI. *NeuroImage*, 16:177–199, 2002.

[8] Y. Assaf and P. Basser. Composite hindered and restricted model of diffusion (CHARMED) MR imaging of the human brain. *NeuroImage*, 27(1):48–58, 2005.

[9] Yaniv Assaf, Raisa Z. Freidlin, Gustavo K. Rohde, and Peter J. Basser. New modeling and experimental framework to characterize hindered and restricted water diffusion in brain white matter. *Magnetic Resonance in Medicine*, 52:965–978, 2004.

[10] Haz-Edine Assemlal, David Tschumperle, Luc Brun, and Kaleem Siddiqi. Recent advances in diffusion mri modeling: Angular and radial reconstruction. *Medical Image Analysis*, 15:369–396, 2011.

[11] Yu Bai and Daniel C. Alexander. Model-based registration to correct for motion between acquisitions in diffusion MR imaging. In *Proceedings of International Symposium on Biomedical Imaging – ISBI*, pages 947–950, Paris, May 2008.

[12] Angelos Barmpoutis, Min Sig Hwang, Dena Howland, John R. Forder, and Baba C. Vemuri. Regularized positive-definite fourth order tensor field estimation from DW-MRI. *NeuroImage*, 45:S153–S162, 2009.

[13] Angelos Barmpoutis, Baba C. Vemuri, Dena Howland, and John R. Forder. Extracting tractosemas from a displacement probability field for tractography for DW-MRI. In Dimitris Metaxas, Leon Axel, Gabor Fichtinger, and Gábor Székely, editors, *Medical Image Computing and Computer-Assisted Intervention – MICCAI 2008*, volume 5241 of *LNCS*, pages 9–16. Springer, 2008.

[14] Peter J. Basser and Derek K. Jones. Diffusion-tensor MRI: theory, experimental design and data analysis - a technical overview. *NMR in Biomedicine*, 15:456–467, 2002.

[15] Peter J. Basser, James Mattiello, and Denis LeBihan. MR diffusion tensor spectroscopy and imaging. *Biophysical Journal*, 66:259–267, 1994.

[16] Peter J. Basser, Sinisa Pajevic, Carlo Pierpaoli, Jeffrey Duda, and Akram Aldroubi. In vivo fiber tractography using DT-MRI data. *Magnetic Resonance in Medicine*, 44:625–632, 2000.

[17] Saurav Basu, Thomas Fletcher, and Ross Whitaker. Rician noise removal in diffusion tensor MRI. In *Medical Image Computing and Computer-Assisted Intervention – MICCAI*, volume 4190 of *LNCS*, pages 117–125. Springer, 2006.

[18] P.G. Batchelor, D.L.G. Hill, D. Atkinson, F. Calamanten, and A. Connelly. Fibre-tracking by solving the diffusion-convection equation. In *Proceedings of International Society of Magnetic Resonance in Medicine (ISMRM)*, volume 10, Honolulu, May 2002.

[19] Philipp G. Batchelor, Derek L.G. Hill, Fernando Calamante, and David Atkinson. Study of connectivity in the brain using the full diffusion tensor from mri. In M.F. Insana and R.M. Leahy, editors, *Proceedings of Information Processing in Medical Imaging: IMPI 2001*, pages 121–133, Davis, June 2001.

[20] Christian Beaulieu. The basis of anisotropic water diffusion in the nervous system - a technical review. *NMR in Biomedicine*, 15:435–455, 2002.

[21] Christian Beaulieu. The biological basis of diffusion tractography. In *Proceedings of International Symposium on Biomedical Imaging (ISBI)*, pages 347–350, Arlington, April 2006.

[22] S.M.A. Becker, K. Tabelow, H.U. Voss, A. Anwander, R.M. Heidemann, and J. Polzehl. Position-orientation adaptive smoothing of diffusion weighted magnetic resonance data (POAS). *Medical Image Analysis*, 16:1142–1155, 2012.

[23] T.E.J. Behrens, H. Johansen Berg, S. Jbabdi, M.F.S. Rushworth, and M.W. Woolrich. Probabilistic diffusion tractography with multiple fibre orientations: What can we gain? *NeuroImage*, 34:144–155, 2007.

[24] T.E.J. Behrens, M.W. Woolrich, M. Jenkinson, H. Johansen-Berg, R.G. Nunes, S. Clare, P.M. Matthews, J.M. Brady, and S.M. Smith. Characterization and propagation of uncertainty in diffusion-weighted MR imaging. *Magnetic Resonance in Medicine*, 50:1077–1088, 2003.

[25] Orjan Bergmann, Gordon Kindlmann, Sharon Peled, and Carl-Fredrik Westin. Two-tensor fiber tractography. In *Proceedings of International Symposium on Biomedical Imaging (ISBI)*, pages 796–799, Washington, April 2007.

[26] D. Le Bihan and E. Breton. Imagerie de diffusion in vivo par résonance magnétique nucléaire. *Compte Rendus de l'Académie de Sciences Paris*, 301:1109–1112, 1985.

[27] Mats Björnemo, Anders Brun, Ron Kikinis, and Carl-Fredrik Westin. Regularized stochastic white matter tractography using diffusion tensor MRI. In T. Dohi and R. Kikinis, editors, *Medical Image Computing and Computer-Assisted Intervention – MICCAI*, volume 2488, pages 435–442, Berlin, 2002. Springer.

[28] Luke Bloy and Ragini Verma. On computing the underlying fiber directions from the diffusion orientation distribution function. In Dimitris Metaxas, Leon Axel, Gabor Fichtinger, and Gábor Székely, editors, *Medical Image Computing and Computer-Assisted Intervention – MICCAI 2008*, volume 5241 of *LNCS*, pages 1–8. Springer, 2008.

[29] Nils Bodammer, Jorn Kaufmann, Martin Kanowski, and Claus Tempelmann. Eddy current correction in diffusion-weighted imaging using pairs of images acquired with opposite diffusion gradient polarity. *Magnetic Resonance in Medicine*, 51:188–193, 2004.

[30] Brian G. Booth and Ghassan Hamarneh. Consistent information content estimation for diffusion tensor MR images. In *Proceedings of Healthcare Informatics, Imaging and Systems Biology (HISB)*, pages 166–173, San Jose, USA, July 2011.

[31] Brian G. Booth and Ghassan Hamarneh. Exact integration of diffusion orientation distribution functions for graph-based diffusion MRI analysis. In *Proc. of ISBI*, pages 935–938, Chicago, USA, 2011.

[32] Brian G. Booth and Ghassan Hamarneh. Multi-region competitive tractography via graph-based random walks. In *Proceedings of Mathematical Methods in Biomedical Image Analysis (MMBIA)*, pages 73–78, Breckenridge, USA, January 2012.

[33] Brian G. Booth and Ghassan Hamarneh. A cross-sectional piecewise constant model for segmenting highly curved fiber tracts in diffusion MR images. In Springer, editor, *Proceedings of Medical Image Computing and Computer-Assisted Intervention (MICCAI)*, pages 469–476, Nagoya, Japan, 2013.

[34] Brian G. Booth and Ghassan Hamarneh. *Medical Imaging: Technology and Applications*, chapter 19: Brain Connectivity Mapping and Analysis using Diffusion MRI, pages 529–563. CRC Press, 2013.

[35] Brian G. Booth and Ghassan Hamarneh. DTI-DeformIt: Generating ground-truth validation data for diffusion tensor image analysis tasks. In *IEEE International Symposium on Biomedical Imaging (IEEE ISBI)*, pages 730–733, Beijing, China, 2014.

[36] Colin Brown, Brian G. Booth, and Ghassan Hamarneh. K-confidence: Assessing uncertainty in tractography using k optimal paths. In *IEEE International Symposium on Biomedical Imaging (IEEE ISBI)*, pages 250–253, San Francisco, USA, 2013.

[37] Colin J. Brown, Brian G. Booth, and Ghassan Hamarneh. Uncertainty in tractography via tract confidence regions. In *Medical Image Computing and Computer-Assisted Intervention Workshop on Computational Diffusion MRI (MICCAI CDMRI)*, pages 13–22, Nagoya, Japan, 2013.

[38] Colin J. Brown, Steven P. Miller, Brian G. Booth, Shawn Andrews, Vann Chau, Kenneth J. Poskitt, and Ghassan Hamarneh. Structural network analysis of brain development in young preterm neonates. *NeuroImage*, 101:667–680, 2014.

[39] Robert Brown. A brief account of microscopical observations made in the months of june, july and august 1827 on the particles contained in the pollen of plants; and on the general existence of active molecules in organic and inorganic bodies. *Philosophical Magazine*, 4:161, 1828.

[40] Ed Bullmore and Olaf Sporns. Complex brain networks: graph theoretical analysis of structural and functional systems. *Nature Review Neuroscience*, 10(3):186–198, March 2009.

[41] Uli Bürgel, Katrin Amunts, Lars Hoemke, Hartmut Mohlberg, Joachim M. Gilsbach, and Karl Zilles. White matter fiber tracts of the human brain: Three-dimensional mapping at microscopic resolution, topography and intersubject variability. *NeuroImage*, 29:1092–1105, 2006.

[42] Jennifer S.W. Campbell, Kaleem Siddiqi, Vladimir V. Rymar, Abbas F. Sadikot, and G. Bruce Pike. Flow-based fiber tracking with diffusion tensor and q-ball data: Validation and comparison to principal diffusion direction techniques. *NeuroImage*, 27:725–736, 2005.

[43] Lin-Ching Chang, Derek K. Jones, and Carlo Pierpaoli. RESTORE: Robust estimation of tensors by outlier rejection. *Magnetic Resonance in Medicine*, 53:1088–1095, 2005.

[44] Bin Chen, Hua Guo, and Allen W. Song. Correction for direction-dependent distortions in diffusion tensor imaging using matched magnetic field maps. *NeuroImage*, 30:121–129, 2006.

[45] Philip A. Cook, Hui Zhang, Suyash P. Awate, and James C. Gee. Atlas-guided probabilistic diffusion-tensor fiber tractography. In *Proceeding of International Symposium on Biomedical Imaging (ISBI)*, pages 951–954, Paris, May 2008.

[46] Steve Crettenand, Stephen D. Meredith, Matthew J. Hoptman, and Richard B. Reilly. Quantitative analysis and comparison of diffusion tensor imaging tractography algorithms. In *Proceedings of Irish Signals and Systems Conference – ISSC*, pages 105–110, Dublin, June 2006.

[47] Alessandro Daducci, Alessandro Dal Palu, Alia Lemkaddem, and Jean-Philippe Thiran. A convex optimization framework for global tractography. In *IEEE International Symposium on Biomedical Imaging (IEEE ISBI)*, pages 524–527, San Francisco, USA, 2013.

[48] M. Descoteaux, R. Deriche, T. R. Knösche, and A. Anwander. Deterministic and probabilistic tractography based on complex fibre orientation distributions. *IEEE Trans. Med. Imag.*, 28(2):269–286, 2009.

[49] Maxime Descoteaux, Elaine Angelino, Shaun Fitzgibbons, and Rachid Deriche. Apparent diffusion coefficients from high angular resolution diffusion imaging: Estimation and applications. *Magnetic Resonance in Medicine*, 56:395–410, 2006.

[50] Maxime Descoteaux, Elaine Angelino, Shaun Fitzgibbons, and Rashid Deriche. Regularized, fast, and robust analytical q-ball imaging. *Magnetic Resonance in Medicine*, 58:497–510, 2007.

[51] Albert Einstein. Uber die von der molekularkinetischen theorie der warme gefordete bewegung von in ruhenden flussigkeiten suspendierten teilchen. *Ann Physik*, 4:549–590, 1905.

[52] Pierre Fillard, Cyril Poupon, and Jean-Francois Mangin. A novel global tractography algorithm based on an adaptive spin glass model. In Springer, editor, *Proceedings of Medical Image Computing and Computer-Assisted Intervention (MICCAI)*, pages 927–934, London, 2009.

[53] Ola Friman, Gunnar Farneback, and Carl-Fredrik Westin. A Bayesian approach for stochastic white matter tractography. *IEEE Transactions on Medical Imaging*, 25(8):965–978, 2006.

[54] Carole Frindel, Marc Robini, Pierre Croisille, and Yue-Min Zhu. Comparison of regularization methods for human cardiac diffusion tensor MRI. *Medical Image Analysis*, 13:405–418, 2009.

[55] J. Gee and D. Alexander. *Visualization and Processing of Tensor Fields*, chapter 20 - Diffusion Tensor Image Registration. Springer, 2005.

[56] Daniel Gembris, Helmut Schumacher, and Dieter Suter. Solving the diffusion equation for fiber tracking in the living human brain. In *Proceedings of International Society of Magnetic Resonance in Medicine (ISMRM)*, page 1529, Glasgow, April 2001.

[57] Arthur C. Guyton. *Textbook of Medical Physiology*. W.B. Saunders, Philadelphia, 8th edition, 1991.

[58] Nathan S. Hageman, Arthur W. Toga, Katherine Narr, and David W. Shattuck. A diffusion tensor imaging tractography algorithm based on navier-stokes fluid mechanics. *IEEE Transactions on Medical Imaging*, 28(3):348–360, 2009.

[59] P. Hagmann, J.-P. Thiran, L. Jonasson, P. Vandergheynst, S. Clarke, P. Maeder, and R. Meuli. DTI mapping of human brain connectivity: statistical fibre tracking and virtual dissection. *NeuroImage*, 19:545–554, 2003.

[60] Ghassan Hamarneh, Chris McIntosh, and Mark Drew. Perception-based visualization of manifold-valued medical images using distance-preserving dimensionality reduction. *IEEE Transactions on Medical Imaging*, 30(7):1314–1327, 2011.

[61] K. M. Hasan, P. J. Basser, D. L. Parker, and A. L. Alexander. Analytical computation of the eigenvalues and eigenvectors in DT-MRI. *J. Mag. Res.*, 152:41–47, 2001.

[62] John C. Haselgrove and James R. Moore. Correction for distortion of echo-planar images used to calculate the apparent diffusion coefficient. *Magnetic Resonance in Medicine*, 36:960–964, 1996.

[63] Y. Iturria-Medina, E.J. Canales-Rodríguez, L. Melie-García, P.A. Valdés-Hernández, E. Martínez-Montes, Y. Alemán-Gómez, and J.M. Sánchez-Bornot. Characterizing brain anatomical connections using diffusion weighted MRI and graph theory. *NeuroImage*, 36:645–660, 2007.

[64] K.M. Jansons and D.C. Alexander. Persistant angular structure: new insights from diffusion magnetic resonance imaging data. *Inverse Problems in Physics*, 19:1031–1046, 2003.

[65] Jens H. Jensen, Joseph A. Helpern, Anita Ramani, Hanzhang Lu, and Kyle Kaczynski. Diffusional kurtosis imaging: The quantification of non-gaussian water diffusion by means of magnetic resonance imaging. *Magnetic Resonance in Medicine*, 53:1432–1440, 2005.

[66] B. Jian and B. C. Vemuri. A unified computational framework for deconvolution to reconstruct multiple fibers from diffusion weighted MRI. *IEEE Trans. Med. Imag.*, 26(11):1464–1471, 2007.

[67] Bing Jian and Baba C. Vemuri. Multi-fiber reconstruction from diffusion MRI using mixture of wisharts and sparse deconvolution. In N. Karssemeijer and B. Lelieveldt, editors, *Proceedings of Image Processing for Medical Imaging (IPMI)*, volume 4584 of *LNCS*, pages 384–395. Springer, 2007.

[68] Bing Jian, Baba C. Vemuri, Evren Özarslan, Paul R. Carney, and Thomas H. Mareci. A novel tensor distribution model for the diffusion-weighted MR signal. *NeuroImage*, 37:164–176, 2007.

[69] Derek K. Jones. Studying connections in the living human brain with diffusion MRI. *Cortex*, 44(8):936–952, September 2008.

[70] Derek K. Jones. Tractography gone wild: Probabilistic fiber tracking using the wild bootstrap with diffusion MRI. *IEEE Transactions on Medical Imaging*, 27(9):1268–1274, September 2008.

[71] Derek K. Jones and Peter J. Basser. ”squashing peanuts and smashing pumpkins”: How noise distorts diffusion-weighted MR data. *Magnetic Resonance in Medicine*, 52:979–993, 2004.

[72] Ning Kang, Jun Zhang, Eric S. Carlson, and Daniel Gembris. White matter fiber tractography via anisotropic diffusion simulation in the human brain. *IEEE Transactions on Medical Imaging*, 24(9):1127–1137, September 2005.

[73] I. Kezele, M. Descoteaux, C. Poupon, F. Poupon, and J.-F. Mangin. Spherical wavelet transform for ODF sharpening. *Medical Image Analysis*, 14:332–342, 2010.

[74] Martin A. Koch, David G. Norris, and Margret Hund-Georgiadis. An investigation of functional and anatomical connectivity using magnetic resonance imaging. *NeuroImage*, 16:241–250, 2002.

[75] B.W. Kreher, I. Mader, and V.G. Kiselev. Gibbs tracking: A novel approach for the reconstruction of neuronal pathways. *Magnetic Resonance in Medicine*, 60:953–963, 2008.

[76] Mariana Lazar and Andrew L. Alexander. Bootstrap white matter tractography (BOOTTRAC). *NeuroImage*, 24:524–532, 2005.

[77] Mariana Lazar, David M. Weinstein, Jay S. Tsuruda, Khader M. Hasan, Konstantinos Arfanakis, M. Elizabeth Meyerand, Benham Badie, Howard A. Rowley, Victor Haughton, Aaron Field, and Andrew L. Alexander. White matter tractography using diffusion tensor deflection. *Human Brain Mapping*, 18:306–321, 2003.

[78] Alexander Leemans and Derek K. Jones. The B-matrix must be rotated when correcting for subject motion in DTI data. *Magnetic Resonance in Medicine*, 61:1336–1349, 2009.

[79] Christophe Lenglet, Rachid Deriche, and Olivier Faugeras. Diffusion tensor magnetic resonance imaging: Brain connectivity mapping. Technical Report 4983, INRIA, October 2003.

[80] Christophe Lenglet, Rachid Deriche, and Olivier Faugeras. Inferring white matter geometry from diffusion tensor MRI: Application to connectivity mapping. In *Proceedings of European Conference on Computer Vision (ECCV)*, pages 127–140, Prague, May 2004.

[81] Alex D. Leow, Siwei Zhu, Katie McMahon, Greig I. de Zubicaray, Matt Meredith, Margie Wright, and Paul M. Thompson. The tensor distribution model. In *Proceedings of the International Symposium on Biomedical Imaging (ISBI)*, pages 863–866, May 2008.

[82] Chunlei Liu, Roland Bammer, Burak Acar, and Michael E. Moseley. Characterizing non-gaussian diffusion by using generalized diffusion tensors. *Magnetic Resonance in Medicine*, 51:924–937, 2004.

[83] J.-F. Mangin, P. Fillard, Y. Cointepas, D. Le Bihan, V. Frouin, and C. Poupon. Toward global tractography. *NeuroImage*, 80:290–296, 2013.

[84] J.-F. Mangin, C. Poupon, C. Clark, D. Le Bihan, and I. Bloch. Distortion correction and robust tensor estimation for MR diffusion imaging. *Medical Image Analysis*, 6:191–198, 2002.

[85] Susumu Mori. John Hopkins Medical Institute: Laboratory of Brain Anatomical MRI, in vivo human database. http://lbam.med.jhmi.edu/, accessed February 2009.

[86] Susumu Mori, Barbara J. Crain, V.P. Chacko, and Peter C.M. van Zijl. Three-dimensional tracking of axonal projections in the brain by magnetic resonance imaging. *Annals of Neurology*, 45(2):265–269, 1999.

[87] Susumu Mori and Peter C.M. van Zijl. Fiber tracking: principles and strategies - a technical review. *Nuclear Magnetic Resonance in Biomedicine*, 15:468–480, 2002.

[88] P. Mukherjee, J.I. Berman, S.W. Chung, C.P. Hess, and R.G. Henry. Diffusion tensor MR imaging and fiber tractography: Theoretic underpinnings. *American Journal of Neuroradiology*, 29:632–641, April 2008.

[89] P. Mukherjee, S.W. Chung, J.I. Berman, C.P. Hess, and R.G. Henry. Diffusion tensor MR imaging and fiber tractography: Technical considerations. *Americal Journal of Neuroradiology*, 29:843–852, May 2008.

[90] K. Krishna Nand, Rafeef Abugharbieh, Brian G. Booth, and Ghassan Hamarneh. Detecting structure in diffusion tensor mr images. In Springer, editor, *Medical Image Computing and Computer-Assisted Intervention (MICCAI)*, volume 6892 of *LNCS*, pages 90–97, Toronto, Canada, 2011.

[91] Paolo G.P. Nucifora, Ragini Verma, Seung-Koo Lee, and Elias R. Melhem. Diffusion-tensor MR imaging and tractography: Exploring brain microstructure and connectivity. *Radiology*, 245(2):367–384, November 2007.

[92] Lauren O'Donnell, Steven Haker, and Carl-Fredrik Westin. New approaches to estimation of white matter connectivity in diffusion tensor mri: Elliptic pdes and geodesics in a tensor-warped space. In *Medical Image Computing and Computer-Assisted Intervention – MICCAI 2002*, pages 459–466, Tokyo, Japan, 2002.

[93] Evren Ozarslan and Thomas H. Mareci. Generalized diffusion tensor imaging and analytical relationships between diffusion tensor imaging and high angular resolution diffusion imaging. *Magnetic Resonance in Medicine*, 50:955–965, 2003.

[94] Evren Ozarslan, Baba C. Vemuri, and Thomas H. Mareci. Generalized scalar measures for diffusion mri using trace, variance, and entropy. *Magnetic Resonance in Medicine*, 53:866–876, 2005.

[95] E. Özerslan, T. Shepherd, B. Vemuri, S. Blackband, and T. Mareci. Resolution of complex tissue microarchitecture using the diffusion orientation transform (DOT). *NeuroImage*, 31(3):1086–1103, 2006.

[96] Sinisa Pajevic and Carlo Pierpaoli. Color schemes to represent the orientation of anisotropic tissues from diffusion tensor data: Application to white matter fiber tract mapping in the human brain. *Magnetic Resonance in Medicine*, 42:526–540, 1999.

[97] Eleftheria Panagiotaki, Torben Schneider, Bernard Siow, Matt G. Hall, Mark F. Lythgoe, and Daniel C. Alexander. Compartment models of the diffusion mr signal in brain white matter: A taxonomy and comparison. *NeuroImage*, 59:2241–2254, 2012.

[98] Geoffrey J.M. Parker, Hamied A. Haroon, and Claudia A.M. Wheeler-Kingshott. A framework for streamline-based probabilistic index of connectivity (PICo) using a structural interpretation of MRI diffusion measurements. *Journal of Magnetic Resonance Imaging*, 18:242–254, 2003.

[99] Geoffrey J.M. Parker, Julia A. Schnabel, Mark R. Symms, David J. Werring, and Gareth J. Barker. Nonlinear smoothing for reduction of systematic and random errors in diffusion tensor imaging. *Journal of Magnetic Resonance Imaging*, 11:702–710, 2000.

[100] Geoffrey J.M. Parker, Claudia A.M. Wheeler-Kingshott, and Gareth J. Barker. Estimating distributed anatomical connectivity using fast marching methods and diffusion tensor imaging. *IEEE Transactions on Medical Imaging*, 21(5):505–512, 2002.

[101] Ofer Pasternak, Nir Sochen, and Peter J. Basser. The effect of metric selection on the analysis of diffusion tensor MRI data. *NeuroImage*, 49:2190–2204, 2010.

[102] Alonso Ramirez-Manzanares, Philip A. Cook, and James C. Gee. A comparison of methods for recovering intra-voxel white matter fiber architecture from clinical diffusion imaging scans. In *Medical Image Computing and Computer-Assisted Intervention – MICCAI*, volume 5241 of *LNCS*, pages 305–312. Springer, 2008.

[103] Yogesh Rathi, Oleg Michailovich, Martha E. Shenton, and Sylvain Bouix. Directional functions for orientation distribution estimation. *Medical Image Analysis*, 13:432–444, 2009.

[104] Carlos Alberola-Lopez Rodrigo de Luis-Garcia and Carl-Fredrik Westin. *Tensors in Image Processing and Computer Vision*, chapter Segmentation of Tensor Fields: Recent Advances and Perspectives. Springer, 2009.

[105] G.K. Rohde, A.S. Barnett, P.J. Basser, S. Marenco, and C. Pierpaoli. Comprehensive approach for correction of motion and distortion in diffusion-weighted MRI. *Magnetic Resonance in Medicine*, 51:103–114, 2004.

[106] Ken E. Sakaie and Mark J. Lowe. Quantitative assessment of motion correction for high angular resolution diffusion imaging. *Magnetic Resonance Imaging*, 28:290–296, 2010.

[107] Peter Savadjiev, Jennifer S.W. Campbell, G. Bruce Pike, and Kaleem Siddiqi. 3d curve inference for diffusion MRI regularization and fibre tractography. *Medical Image Analysis*, 10:799–813, 2006.

[108] Giovanni Sebastiani, Francesco de Pasquale, and Piero Barone. Quantifying human brain connectivity from diffusion tensor MRI. *Journal of Mathematical Imaging and Vision*, 25:227–244, 2006.

[109] S.N. Sotiropoulos, L. Bai, P.S. Morgan, C.S. Constantinescu, and C.R. Tench. Brain tractography using Q-ball imaging and graph theory: Improved connectivities through fibre crossings via a model-based approach. *NeuroImage*, 49:2444–2456, 2010.

[110] E.O. Stejskal and J.E. Tanner. Spin diffusion measurements: Spin echoes in the presence of a time-dependent field gradient. *The Journal of Chemical Physics*, 42(1):288–292, January 1965.

[111] J-Donald Tournier, Fernando Calamante, and Alan Connelly. Robust determination of the fibre orientation distribution in diffusion MRI: Non-negativity constrained super-resolved spherical deconvolution. *NeuroImage*, 35:1459–1472, 2007.

[112] J.-Donald Tournier, Fernando Calamante, David G. Gadian, and Alan Connelly. Diffusion-weighted magnetic resonance imaging fibre tracking using a front evolution algorithm. *NeuroImage*, 20:276–288, 2003.

[113] Antonio Tristan-Vega and Santiago Aja-Fernandez. DWI filtering using joint information for DTI and HARDI. *Medical Image Analysis*, 14:205–218, 2010.

[114] Theodore P. Trouard, Yashvinder Sabharwal, Maria I. Altbach, and Arthur F. Gmitro. Analysis and comparison of motion correction techniques in diffusion-weighted imaging. *Journal of Magnetic Resonance Imaging*, 6(6):925–935, 1996.

[115] David S. Tuch. Q-ball imaging. *Magnetic Resonance in Medicine*, 52:1358–1372, 2004.

[116] David S. Tuch, Timothy G. Reese, Mette R. Wiegell, Nikos Makris, John W. Belliveau, and Van J. Wedeen. High angular resolution diffusion imaging reveals intravoxel white matter fiber heterogeneity. *Magnetic Resonance in Medicine*, 48:577–582, 2002.

[117] Elisabeth A.H. von dem Hagen and R. Mark Henkelman. Orientational diffusion reflects fiber structure within a voxel. *Magnetic Resonance in Medicine*, 48:454–459, 2002.

[118] Zhizhou Wang, Baba C. Vemuri, Yunmei Chen, and Thomas H. Mareci. A constrained variational principle for direct estimation and smoothing of the diffusion tensor field from complex DWI. *IEEE Transactions on Medical Imaging*, 23(8):930–939, 2004.

[119] V. Wedeen, T. Reese, D. Tuch, M. Wiegel, J.-G. Dou, R. Weiskoff, and D. Chessler. Mapping fiber orientation spectra in cerebral white matter with fourier-transform diffusion MRI. In *Proceedings of the International Society of Magnetic Resonance in Medicine*, page 82, Denver, April 2000.

[120] C.-F. Westin, S.E. Maier, H. Mamata, A. Nabavi, F.A. Jolesz, and R. Kikinis. Processing and visualization for diffusion tensor mri. *Medical Image Analysis*, 6:93–108, 2002.

[121] Brandon Whitcher, David S. Tuch, Jonathan J. Wisco, A. Gregory Sorensen, and Liqun Wang. Using the wild bootstrap to quantify uncertainty in diffusion tensor imaging. *Human Brain Mapping*, 29:346–362, 2008.

[122] Nicolas Wiest-Daessle, Sylvain Prima, Pierrick Coupe, Sean Patrick Morrissey, and Christian Barillot. Non-local means variants for denoising of diffusion-weighted and diffusion tensor MRI. In *Medical Image Computing and Computer-Assisted Intervention – MICCAI*, volume 4792 of *LNCS*, pages 344–351. Springer, 2007.

[123] A. Zalesky. DT-MRI fiber tracking: A shortest paths approach. *IEEE Trans. Med. Imag.*, 27(10):1458–1571, 2008.

[124] Fan Zhang, Edwin R. Handcock, Casey Goodlett, and Guido Gerig. Probabilistic white matter fiber tracking using particle filtering and von Mises-Fisher sampling. *Medical Image Analysis*, 13:5–18, 2009.

[125] Jun Zhang, Hao Ji, Ning Kang, and Ning Cao. Fiber tractography in diffusion tensor magnetic resonance imaging: A survey and beyond. Technical Report 437-05, University of Kentucky, April 2005.

[126] Jun Zhang, Ning Kang, and Stephen E. Rose. Approximating anatomical brain connectivity with diffusion tensor MRI using kernel-based diffusion simulations. In *Proceedings of Information Processing for Medical Imaging – IPMI*, volume 3565 of *LNCS*, pages 64–75. Springer, 2005.